doi:10.26443/seismica.v5i1.1728

Seismic characterization of the subsurface and anthropogenic noise at the LUNA Moon analog facility

Brigitte Knapmeyer-Endrun * [1], **Martin Knapmeyer** [2], **Olav Cornelius** [3], **Hans-Herbert Fischer** [4], **Maria Hallinger** [1], **Cinzia Fantinati** [1], **Oliver Küchemann** [1], **Michael Maibaum** [1]

[1]Microgravity User Support Center, German Aerospace Center (DLR), Cologne, Germany, [2]Institute for Planetary Research, German Aerospace Center (DLR), Berlin, Germany, [3]Department of Earth and Planetary Sciences, Institute of Geophysics, ETH Zurich, Zurich, Switzerland, [4]retired, formerly at: Microgravity User Support Center, German Aerospace Center (DLR), Cologne, Germany

Author contributions: *Conceptualization*: Brigitte Knapmeyer-Endrun, Martin Knapmeyer. *Methodology*: Brigitte Knapmeyer-Endrun. *Software*: Brigitte Knapmeyer-Endrun, Martin Knapmeyer. *Formal Analysis*: Brigitte Knapmeyer-Endrun, Olav Cornelius. *Investigation*: Brigitte Knapmeyer-Endrun, Martin Knapmeyer, Hans-Herbert Fischer, Maria Hallinger, Cinzia Fantinati, Oliver Küchemann, Michael Maibaum. *Writing - Original draft*: Brigitte Knapmeyer-Endrun. *Writing - Review & Editing*: Martin Knapmeyer, Olav Cornelius, Hans-Herbert Fischer, Michael Maibaum. *Visualization*: Brigitte Knapmeyer-Endrun, Martin Knapmeyer. *Supervision*: Brigitte Knapmeyer-Endrun, Martin Knapmeyer. *Project administration*: Michael Maibaum.

Abstract The increased interest in crewed and robotic lunar exploration results in a need for high-quality testbeds for instruments, experiments—including seismological ones—and procedures, and for operations training. The LUNA analog facility is a new large-scale testbed on the DLR campus in Cologne, Germany, i.e. located in an urban environment that includes traffic, heavy machinery, and a neighboring international airport. We perform the first characterization of the site and its ambient wavefield, with a focus on anthropogenic signals, as relevant background information for future users of LUNA. Combining active and passive seismic measurements, we derive velocity models for the site down to the bedrock at 152 ± 13 m depth. We provide a preliminary characterization of the ambient noise on campus and discuss and interpret examples of common anthropogenic signals in detail, demonstrating their use e.g. for traffic monitoring with a single station, or as a repeating seismic source. This study showcases how relevant information for future seismological users of a planetary analog facility can be derived with comparatively limited means, the potential of single-station seismology for monitoring airborne and ground traffic, and hints at possible uses of the future permanent seismometer in LUNA.

Production Editor: Andrea Llenos
Handling Editor: György Hetenyi
Copy & Layout Editor: Hannah F. Mark

Received: May 20, 2025
Accepted: January 16, 2026
Published: February 4, 2026

Non-technical summary The newly increased interest in lunar science and exploration means that facilities to test instruments, experiments, and operation concepts before sending robots or humans to the Moon have also gained importance. One such facility, LUNA, with a 700 m^2 testbed filled with lunar regolith simulant, has recently been inaugurated by ESA and DLR in Cologne. Seismology has played an important role during the Apollo years to determine the interior structure and seismicity of the Moon and might in the future also be used to detect near-surface resources or monitor hazards to astronauts and built infrastructure. To help future users of LUNA who want to test seismic instrumentation better understand their data, we determined the subsurface to 200 m depth beneath LUNA's location using a combination of seismic methods. We characterized the background ambient noise wavefield on the campus to aid future users in the design of their campaigns, and also described and analyzed some common man-made signals, e.g., by cars, a bus, an airplane, and a helicopter, that future users are likely to encounter in their data and could potentially utilize. Finally, we show that the permanent seismometer that will be installed in LUNA will provide useful recordings of distant earthquakes, and might also see some small local quakes.

1 Introduction

To support the growing international interest in lunar exploration, the German Aerospace Center (DLR) and the European Space Agency (ESA) have inaugurated a large-scale testbed facility, LUNA, on the DLR campus in Cologne, Germany, in September 2024. LUNA allows to develop, demonstrate and validate new technologies and operational concepts for crewed as well as robotic missions, including instrument tests, in a controlled, standardized environment (Casini et al., 2020), i.e. the 700 m^2 regolith yard filled with lunar mare regolith simulant EAC-1A (Engelschiøn et al., 2020; Zemeny et al., 2024; Vrettos et al., 2026). During the Apollo missions in the 1960s and 1970s, active and passive seismic experiments exemplified a very successful application of geophysical exploration to the Moon (for a recent review, see Garcia et al., 2019), with new insights still being derived from these data sets today (e.g., Turner et al., 2022; Civilini et al., 2023; Imazato et al., 2023; Keil et al., 2024; Onodera, 2024). Currently, new lunar seismometers are in development (e.g., Nunn et al., 2021; Erwin et al., 2021; de Paula et al., 2023), and three-component accelerometer data has recently been collected on the Moon as part of the Indian Space Re-

*Corresponding author: brigitte.knapmeyer-endrun@dlr.de

search Organization's (ISRO's) Chandrayaan-3 mission (John et al., 2024). More broad-band and longer-term seismometer deployments are scheduled for the Far-side Seismic Suite (FSS) on Commercial Lunar Payload Services (CLPS) flight CP-12 (Aboobaker et al., 2024), the Lunar Environmental Monitoring Station (LEMS) on Artemis III, and the lunar seismograph (LS) on Chang'E 7 (Wang et al., 2023). In addition, rover-based seismic profiling has been proposed to investigate the shallow subsurface of the Moon (Tsuji et al., 2023), and the use of fiber optic cables for distributed acoustic sensing (DAS) on the Moon is being investigated (Wu et al., 2024; Zhai et al., 2024; Harmon et al., 2024). To support future testing of seismological instruments and experiments, the planned outfitting of LUNA includes a permanent broad-band seismometer (Nanometrics Trillium compact 120 s) on the concrete floor of the testbed, and 500 m of fiber-optic cable, including an engineered fiber, deployed in a grid-like pattern below the regolith.

Cologne is located in the Lower Rhine Embayment (LRE) on thick Tertiary to Quaternary sediments above a Devonian basement (Schäfer et al., 2005). Site effects are expected, and information on the subsurface velocity structure below LUNA is of interest for the interpretation of future experiments at the facility. NW-SE trending faults divide the LRE into a number of blocks that are subsiding individually, with up to 2000 m of sedimentary cover in the Roer Valley in the west of the basin. Below the city of Cologne, the sedimentary thickness varies between 50 m and more than 300 m, increasing to the SW (Tyagunov et al., 2006). Some ground truth is available in the form of borehole stratigraphy at several locations on the 55 hectare DLR campus (Geologischer Dienst NRW, 2023), though not directly at the LUNA site; however, no additional borehole logs, to e.g. provide in-situ velocity information, are available.

Closest to the location of LUNA are boreholes DABO_207054, approximately 280 m to the west, and DABO_207052, about 250 m to the west-north-west (Fig. 1). While most of the boreholes on campus, including DABO_207054, extend to less than 20 m depth, DABO_207052 reached a length of 210 m and found Devonian strata below 170.1 m. This borehole also evidenced Holocene sands and construction waste in the uppermost meter. Stratigraphic interpretation of both boreholes shows the Early Pleistocene unconformity in the Cologne block (Schäfer et al., 2005), where Oligocene clays are discordantly overlain by Mid-Pleistocene gravel and sand, at 18.5 m and 23.8 m depth, respectively. At DABO_207052, Oligocene clays and silts, containing narrow bands of coal and a thin layer of sandstone at around 118 m depth, continue all the way down to the Devonian strata. The federal state of North Rhine-Westphalia also runs a groundwater gauge station on the DLR campus, for which no exact coordinates are available (Land NRW, 2023). The available data indicate an average groundwater level of 16.5 $\pm$ 1 m beneath the local surface, with a potentially measurable influence on P-wave velocities.

Additional a priori information consists of ambient vibration horizontal-to-vertical spectral ratio (HVSR) measurements in the Cologne area (Parolai et al., 2004), including at an unspecified site at the western end of the DLR campus, about 1 km away from LUNA. For that site, a peak frequency of 0.6 to 0.67 Hz is reported, which is translated into a bedrock depth of 200 to 240 m by Parolai et al. (2004) via an empirical relation (Parolai et al., 2002), suggesting a significant westerly slope in the sediment-bedrock interface across the campus when compared to the borehole data. However, Parolai et al. (2002) are not the only authors to propose a relation between S-wave velocity and depth for the sediments of the LRE (e.g., Budny, 1984; Ibs-von Seht and Wohlenberg, 1999; Scherbaum et al., 2003), or directly between HVSR peak frequency and bedrock depth (e.g., Finger et al., 2025). Hinzen et al. (2004) showed that there is a high variability between the different relations, with the equations by Parolai et al. (2002) leading to significantly higher velocities than derived in other studies, especially when considering depths in excess of 400 m, and thus resulting in significantly higher estimates of bedrock depth from HVSR peak frequencies. Accordingly, additional in situ measurements are required to actually link the available stratigraphic information to a sub-surface velocity model and to determine the bedrock depth at LUNA.

The location of LUNA was chosen based on operational and logistic considerations, i.e. vicinity to ESA's European Astronaut Center (EAC, Fig. 1) and the DLR Institutes for Aerospace Medicine, Materials Research, and Space Operations and Astronaut Training, not considering the suitability for a seismic station. Hence, the LUNA seismometer will record data in a particular urban environment: More than 1800 employees work on the DLR campus and generate traffic, heavy machinery is used for research (e.g., wind tunnels, jet engine test stands, human-sized centrifuges), and CGN international airport borders the premises to the north and east; the nearest runway is, at its closest point, about 1 km away from LUNA. As all of these noise sources might influence future tests and experiments with seismological instruments in LUNA, the expected noise level and its temporal variability as well as the characteristics of common noise sources are important for potential users, both to know what to expect when planning an campaign, as well as to better understand and interpret the recorded data. Accordingly, we provide an initial characterization of the noise level on site and an assessment of common anthropogenic signals and how they might be utilized, with a focus on how they can be recognized and differentiated with a single broad-band seismometer that will be permanently installed in LUNA.

2 Subsurface structure

2.1 Data and methods

Before the construction of LUNA, the area was used as a parking lot. Using 24 vertical-component geophones and 5 shot positions, a seismic refraction profile of 46 m length was recorded along the western boundary of the parking lot in February 2023 (Fig. 1, Supplemental Fig. S1a, b). First onsets, including uncertainties, were picked on all traces. Since no clear differences be-

Figure 1 Aerial photography of the Cologne region, with inset, marked by red rectangle in overview picture, showing the measurement location in detail. Blue line indicates seismic refraction profile, while red triangles indicate seismometer array at future LUNA location (approximately outlined by white dashed lines), and orange diamond is the location of the long-term test installations (either broad-band or short-period station). Pink labeled marks indicate the two boreholes. Orthoimage of region obtained from https://www.geoportal.nrw under licence https://www.govdata.de/dl-de/zero-2-0. Orthoimage of measurement location obtained from https://www.bezreg-koeln.nrw.de/geobasis-nrw/tim-online, Bezirksregierung Köln.

tween the travel times for various shot positions were apparent, data from all shots were combined in a single travel-time vs. offset plot for interpretation (Supplemental Fig. S2). Assuming no lateral variations in structure, P-wave velocities and layer thicknesses were determined from slopes and intercept times, respectively, of lines fit by minimizing the least-squares residual, with uncertainty determined from bootstrapping over 10,000 realizations. The results were used to constrain the parameter space for the subsequent inversion of the surface wave data.

Data from a shot point at a larger offset from the profile, at 52.9 m, was used for multi-channel analysis of surface waves (MASW, Park et al., 1999, Supplemental Fig. S1c). We used MASWaves (Olafsdottir et al., 2018) to derive a dispersion curve, covering frequencies between 9 Hz and 26 Hz, for the inversion (Supplemental Fig. S3).

After the concrete cover of the parking lot had been removed, but before the construction of LUNA, a dedicated measurement with four short-period seismometers (Lennartz Le-3Dlite, eigenperiod 1s) in a Y-shaped array of 8 m radius was performed at the future LUNA location during three days in August 2023 (Fig. 1). The central station of the short-period array was enhanced by placing a Nanometrics Trillium compact 120 s broadband sensor next to the short-period seismometer. A dispersion curve was extracted from the array data by high- resolution three-component Rayleigh beam forming (RTBF, Wathelet et al., 2018), as implemented in Geopsy (Wathelet et al., 2020). This dispersion curve shows good agreement with the MASW results within the frequency band covered by both, and extends to frequencies of about 5.5 Hz (Supplemental Fig. S3). Results from MASW and RTBF were hence combined into a single Rayleigh wave dispersion curve. As discussed in Wathelet et al. (2018), using the directional information contained in array recordings allows us to distinguish between retrograde and prograde Rayleigh waves, producing an estimate of the signed ellipticity angle in addition to the dispersion curve from RTBF, whereas single-station methods can only provide an estimate of the absolute ellipticity value. Since the signed ellipticity angle is derived from beam forming, it is subject to the same constraints on resolution given by the array layout as the corresponding dispersion curve. Hence, we included the signed ellipticity angle from RTBF over the same frequency band as the Rayleigh wave dispersion

curve in the inversion.

Additionally, three-component spatial autocorrelation functions (SPAC, Aki, 1957; Köhler et al., 2007, Supplemental Fig. S4) were computed for two sets of interstation distances, with radii of 7 to 9 m and 13 to 15 m, respectively. HVSR (Nakamura, 1989; Bonnefoy-Claudet et al., 2006) were derived as well, but since their inversion in terms of Rayleigh wave ellipticity might be biased by the contribution of other wave types to the ambient wavefield (e.g. Bonnefoy-Claudet et al., 2008), we also applied RayDec (Supplemental Fig. S5a). RayDec aims to focus the analysis on time windows dominated by Rayleigh waves, thus providing a less biased estimate of Rayleigh wave ellipticity (Hobiger et al., 2009). Hence, the RayDec curve was used as inversion target.

The dispersion curve was inverted jointly with Rayleigh wave ellipticity information from both RTBF and RayDec, and SPAC using the Neighborhood Algorithm (Sambridge, 1999), a stochastic direct search method, as implemented in the dinver software (Wathelet, 2008). To reduce computational burden, we resampled the various data sets to the same 100 logarithmically distributed frequencies between 0.2 and 26 Hz. We used nearly equal weights for the various input data, with a slightly higher significance for the dispersion curve, i.e. setting weights to 0.4, 0.3 and 0.3 for the dispersion curve, the ellipticity data, and the SPAC curves. Additionally, we constrained Poisson's ratio ν to a value between 0.2 and 0.5 for each layer during the inversion and allowed for a velocity increase following a power law within the second and third layer. As result, we show the combined output of five runs of the Neighborhood Algorithm, starting with different random seeds, each run generating 40,000 models, based on 50 initial random starting models.

The broad-band seismometer intended for installation in LUNA was tested in the building housing DLR's Microgravity User Support Center (MUSC) about 340 m to the west-north-west of LUNA (Fig. 1), providing continuous data for 7 weeks between June and August 2023, and for 17 weeks between December 2023 and April 2024. We also performed HVSR and RayDec analysis with this data set for comparison (Supplemental Fig. S5b).

More details on the data sets and analysis methods are provided in Supplemental Section S1.

2.2 Results

The refraction seismic results were considered independently from the array data. The data point to three layers with increasing velocities within the uppermost 15 m (Supplementary Fig. S2). From the inverse slopes of the travel time curves, P-wave velocities (v_P) of the three layers were determined as listed in Tab. 1. These results were used to constrain the v_P range and the depth of the first two discontinuities in the surface wave inversions, whereas the constraints on S-wave velocity (v_S) were set rather wide (Fig. 2a).

While the refraction data only constrain shallow v_P, complimentary information on the depth to the bedrock is contained in the Rayleigh wave ellipticity peak. Hobiger et al. (2012) illustrate that inverting Rayleigh wave ellipticity alone suffers from a depth-velocity trade-off, though, and demonstrate that this can be resolved by including other data, i.e. dispersion or autocorrelation curves. Hobiger et al. (2012) also show that the right flank of the ellipticity curve, together with the peak frequency, is best suited to constrain subsurface structure. Here, we also included part of the left flank to better constrain the peak frequency at 0.76 Hz, but excluded the peak itself (Fig. 2e), since the peak amplitude predicted by forward calculations is often not reached in actual measured data, even for tests using synthetic seismograms (e.g., Knapmeyer-Endrun et al., 2017). In addition, we include the signed ellipticity angle from RTBF that covers higher frequencies (Fig. 2d). The negative values between 5.5 and 16 Hz indicate retrograde particle motion, which is expected for the fundamental mode Rayleigh wave at frequencies above the H/V trough frequency (Maranò et al., 2017). Note that measurements in the MUSC building result in a lower peak frequency of 0.68 Hz (Supplemental Fig. S5b), closer to the previous measurement in the west of the DLR campus (Parolai et al., 2002), but are obtained about 100 m away from a borehole with 170.1 m bedrock depth, as opposed to the minimum bedrock depth of 200 m derived by Parolai et al. (2002).

Layer No.	Thickness [m]	v_P [m/s]
1	1.63 ± 0.3	533 ± 42
2	12.9 ± 1.6	750 ± 8
3	–	2380 ± 544

Table 1 Results of refraction seismic profile. Velocities are derived from the slope of lines in Supplemental Fig. S2, and layer thicknesses are calculated from intercept times and velocities.

The inversion results are displayed in Fig. 2 in terms of fit to the input data, and the resulting velocity models. The fit to all data points is reasonable. The resulting velocity models indicate that v_P is not well constrained by surface waves, as the v_P model is not improved compared to the constraints derived from the refraction data that were used to set the boundaries of the explored parameter space. On the other hand, v_S is fairly well constrained by the data.

The low-velocity topmost layer of the model to about 2 m depth likely consists of soil and backfill. v_P in the second layer, extending to about 14.5 ± 1.9 m depth, is within the velocity range derived for dry sand or gravel at corresponding depths in the LRE, while expected velocities for dry clay would be larger (Budny, 1984, Fig. 2b). v_P increases markedly below, at a depth that, based on borehole information, could correlate both with the Early Pleistocene unconformity or with the groundwater table. Comparison with compiled velocities for the various sediments in the LRE indicates that dry sands or clays are significantly slower than what is measured here, with velocities below 1200 m/s at the top of the layer (Budny, 1984, Fig. 2b), whereas water saturated sands and clays reach velocities above 2000 m/s. Accordingly, water saturation is required to explain the

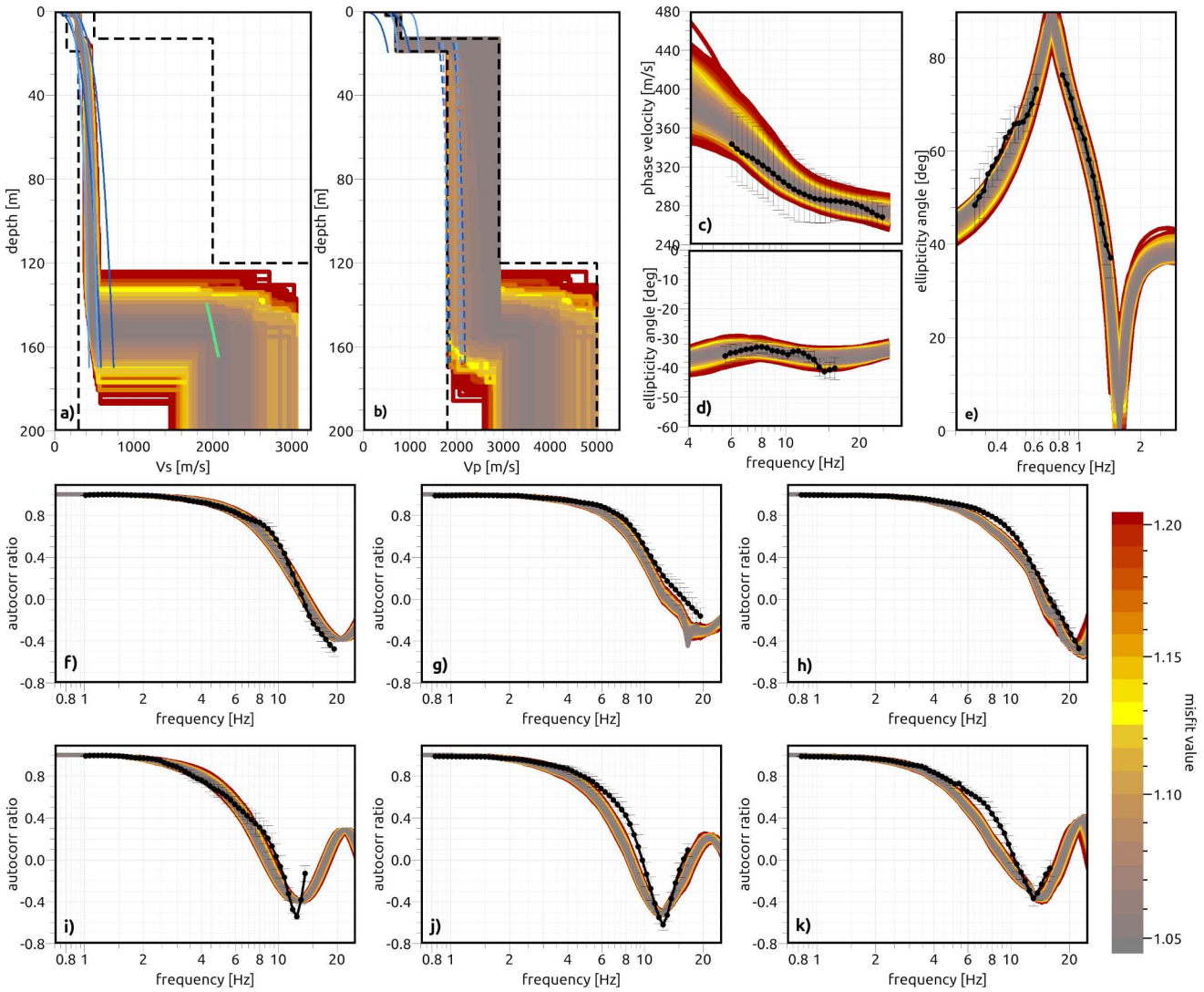

Figure 2 Inversion results for subsurface structure beneath LUNA. S- and P-wave velocity models are shown in (a) and (b), where dashed black lines outline the parameter space allowed in the inversion. Corresponding fits to the data are shown in (c) for the Rayleigh wave fundamental mode dispersion curve, in (d) for the signed ellipticity angle obtained from RTBF, in (e) for the ellipticity angle (absolute value) as obtained from RayDec, and in (f)–(k) for the spatial autocorrelation curves. Here, (f), (g), and (h) are the vertical, radial, and transverse component for the first ring with a radius of 7 to 9 m, and (i), (j), and (k) are the vertical, radial, and transverse component for the second ring with a radius of 13 to 15 m. The dark blue lines in (a) and (b) refer to the predicted velocity range for sands from Budny (1984), whereas the light blue lines refer to the range for clay. In (b), the solid lines are for the vadose zone, whereas the dashed lines are for the phreatic zone, i.e. below the groundwater table. S-wave velocities do not vary with water saturation, so there is only a single type of line in (a). The solid light green line in (a) indicates the bedrock S-wave velocity as predicted by equation 2 (Parolai et al., 2002).

measured v_P below about 15 m.

Notably, the increase in v_S at around 15 m depth it much smaller than the increase in v_P, from about 310 m/s to 380 m/s, so the average v_P/v_S ratio shows a strong increase, from about 2.4 to 5 or more, corresponding to ν of around 0.39 and above 0.47. Similar values are described in the literature for sediments, with values as high as 0.49 for saturated clays (see list in Salem, 2000), and somewhat lower values between 0.25 and 0.4 for sands (see list in Essien et al., 2014). On the other hand, the transition from sand to clay alone cannot explain the observed increase in ν as ν of unsaturated clay is actually lower than that of sand (Essien et al., 2014). Additionally, v_S for sands according to Budny (1984) increases with depth more strongly than for clay and shows little overlap with the inversion results for depths below 120 m, which are around 450 to 500 m/s (Fig. 2a).

Incorporating the prior geological information, the velocity models can be explained by the transition from Pleistocene sands to Oligocene clays and the groundwater table around 15 m depth. The depth to the Pleistocene unconformity varies by more than 5 m between two boreholes on the campus separated by less than 100 m, with shallower depth to the south, so local thinning of the Mid-Pleistocene sand and gravel layer by another 2 to 6 m at the location of LUNA is not unreasonable. The available information on the groundwater level, on

the other hand, overlaps with the derived depth of the layer boundary.

The obtained depth to the bedrock is 152 ± 13 m. This is notably shallower than the depth derived by Parolai et al. (2004) for a location in the west of the DLR campus. However, this depth was not derived by a Monte-Carlo-style inversion of data for a velocity model, but by applying an empirical relation linking bedrock depth to measured HVSR peak frequency (Parolai et al., 2002). Using that equation and the observed peak frequency of 0.76 Hz results in an interface depth of 165 m, which is the upper limit of the depths derived in our inversion for the location of LUNA, whereas the peak frequency of 0.68 Hz measured in the MUSC building would correspond to a depth of 195 m. This is at odds with the ground truth information of 170.1 m from the neighboring borehole, and we also note that the velocity-depth relation provided by Parolai et al. (2002) shows close agreement with the upper limit of sand velocities from Budny (1984), i.e. is faster than what we obtain for depth between 70 and 140 m (Fig. 2a). Accordingly, even for the comparatively shallow bedrock depths at the LUNA location, the relation by Parolai et al. (2002) results in an overestimation of sediment thickness.

On the other hand, using the relation between HVSR peak frequency f and bedrock depth h recently derived for the Weisweiler area to the west-south-west of Cologne (Finger et al., 2025)

$$h = \frac{400}{3.57 \times f} \tag{1}$$

we obtain depths of 147 m for LUNA and 164 m for the MUSC building. This is well within the range of the inversion results and close to the borehole information. Based on this relation, the bedrock is likely at 167 to 187 m depth in the west of the campus, i.e. 30 to 50 m shallower than previously estimated.

The relation between bedrock S-wave velocity v_{sb} and h also mentioned by Parolai et al. (2002)

$$v_{sb} = 210 \times (1 + h)^{0.448} \tag{2}$$

leads to velocities of 1920 to 2075 m/s for a bedrock depth of 152 ± 13 m, consistent with the inversion results (Fig. 2a). For the bedrock, the inverted v_P and v_S are consistent with a v_P/v_S ratio of 1.75, close to the standard often assumed for rocks.

3 Ambient noise

3.1 Data and methods

The long-term recordings in the MUSC building are best suited, both in terms of duration and frequency band covered, to get a general impression of the background noise level on campus. These recordings represent the longest time-series available for a location on the campus at the time of writing, and though they were not obtained at the location of or within LUNA, they still provide an indication on the general noise level, especially due to anthropogenic sources, and its variability on site. This information is important for future instrument tests in LUNA and planning e.g. the timing of measurements to include intervals with lower noise. We calculated probabilistic power spectral densities (PPSD) from the data using the implementation in ObsPy (The ObsPy Development Team, 2022) and the default settings. For comparison, PPSD were also calculated for the broad-band station included in the array deployment on the LUNA site, covering only approximately 3 days in time. We used SeismoRMS (Lecocq et al., 2020b) to investigate the temporal variability in the noise wavefield at anthropogenic frequencies in the long-term recordings. Additionally, since the sensor location was next to a part of a road that was frequented by a bus, the quasi-static deformation signals caused by the bus are analyzed in terms of elastic parameters of the subsurface, based on the Boussinesq point-load solution (Boussinesq, 1885). A similar approach could be used for regolith characterization during future tests involving rovers in LUNA, or even on the Moon, in a comparable fashion to the analysis of quasi-static deformation due to Martian dust-devils by InSight (Lognonné et al., 2020; Murdoch et al., 2021).

We also analyzed the array data in terms of transient signals generated by the most common sources on or near the campus, cars and airborne traffic. These signals are observed frequently in the data, with more than 100 signatures of cars driving by the future location of LUNA identified during the one complete work day covered by the array measurements, and over 250 signals related to airplanes found in the 1.75 days analysed in detail. Accordingly, future seismic campaigns in LUNA will certainly observe these signals, should be able to identify them to prevent any misinterpretation of their data, and might even use them as repeatable sources. We investigated the creation of the car-generated signals by locating their origin, using both array-based and single-station methods, which also makes them suitable for speed monitoring, and give examples for the analysis of flyby signals (e.g. Eibl et al., 2015).

More details on the analysis of specific transient signal types are given in the respective sections.

3.2 Results for the background wave-field

PPSD generally show good agreement between the long-term data (Fig. 3a) and the short-term deployment at the future location of LUNA (Fig. 3b), except at low frequencies due to the non-optimal installation on soil. In general, since the same road passes by both MUSC and the future location of LUNA and other noise sources both at high frequencies like airplanes at CGN and at low frequencies like the oceanic microseisms are identical, we expect the measurements in the MUSC building to provide a reasonable approximation of what is to be expected in LUNA. Sources specific to the LUNA building, e.g. the crane within the hall or the effect of wind impacting the tall walls of the hall, can only be investigated with data from the final location of the permanent seismometer in LUNA, though. The vertical-component PPSD (Fig. 3) shows an elevated noise level, partly above the new high noise model (Peterson, 1993), above 1 Hz. This is to be expected since ambient noise above about 1

Hz is dominated by human activities (Bonnefoy-Claudet et al., 2006), and the DLR campus as well as the CGN airport, the air-force barracks, and the Cologne district of Wahn are all near-by sources of anthropogenic noise. The PPSD exhibit some variability in the frequency range above 1 Hz, with acceleration amplitudes during different time windows varying by more than 15 dB. The temporal variability in this frequency band is investigated in more detail below. Due to the smoothing involved in the calculation of the spectra, individual contributions to the high-frequency noise are not resolved here.

Below 1 Hz, the ambient noise level lies well below the new high noise model and is often less than 10 dB above the new low noise model between 0.3 Hz and 0.05 Hz during summer-time (Fig. 3). During winter time, the noise level in the microseismic band increases by about 15 dB, though, with a clear spectral peak for the secondary oceanic microseism (Supplemental Fig. S6). Below about 0.04 Hz, the power spectral densities show a consistent trend independent of season and often lie below -160 dB. PPSD for the horizontal components show a similar behavior, with additional noise below 0.08 Hz. Based on these observations, human activities make observations of small signals at high frequencies, e.g., due to local earthquakes, challenging on the DLR campus, whereas a good performance is expected at long periods for the future permanent station in LUNA. Examples of both teleseismic and local earthquake recordings during the long-term deployment are given in Supplemental Figs S8 and S9 and discussed in Supplemental Section S2.

The temporal variability in average vertical displacement amplitudes between 4 and 20 Hz is investigated in more detail in Fig. 4, where values are shown at a half-hourly rate for the time between December, 21st 2023 and April, 22nd 2024, in a similar fashion as in Lecocq et al. (2020a). The noise level shows clear variations between day and night time and between weekdays and weekends or holidays, as also observed at other seismic stations within cities (e.g., Groos and Ritter, 2009; Díaz et al., 2017; Green et al., 2017). The day-time noise level on working days, between 6:30 am and 5:30 pm local time, is on average twice as high as the night-time level. Weekends tend to be even more quiet: while the average night-time noise level is about 12 nm, the lowest noise level is measured during the nights from Saturdays to Sundays at about 9 nm. A further reduction is observed during the Christmas holidays (December 23rd to January 2nd), when DLR was basically closed, and the night time noise level is below 7 nm. During the first week of January, only limited personnel was back onsite, as witnessed by the comparatively low noise level during that week. Other notable events include Easter holidays (March 29th to April 1st) and Carnival Monday (February 12th), which, in Cologne, is also a day off at DLR. In January, after the holidays, noise levels were notably higher on workdays in the afternoon and evening, i.e. between 3 pm and 9.30 pm. This can be attributed to a continuous noise source with a broad frequency peak between 5 and 6.5 Hz, generating energy across the whole band between 2 and 13 Hz, with clear start and stop times (Supplemental Figure S7). The machinery acting as this source is currently unidentified; we can however exclude the wind tunnel (Supplemental Fig. S10c), which produces transient signals with energy to much higher frequencies, and the test stand for jet engines based on its activity schedule. A potential future measurement campaign with multiple sensors distributed across the campus could help in pinpointing the location and hence allowing the identification of this type of noise source.

3.3 Transient sources

Fig. 5 provides a closer look at individual high-frequency noise sources from our array measurement at the future location of LUNA. Data shown are typical for a work-day with elevated anthropogenic noise. Narrow spectral bands that are excited continuously, e.g., at 1.9 Hz, 6.1 Hz (with a 12.2 Hz harmonic), 27.3 Hz and 49 Hz, can be attributed to machinery. Noise at 60.6 Hz is excited periodically, with activity of 4.5 to 11 min duration separated by breaks of 7 to 13 min, pointing to a machine with on-off cycles, e.g., air-conditioning in a close-by building. Other frequency bands linked to the activation of machinery are only observed part of the time, e.g., adjacent lines at 24.7 and 24.9 Hz that are only observed until about 12:05 pm. While these bands are also observed on other days, there is no clear pattern to their start or end times or duration, and they are only one example for narrow-band, discontinuous signals generated by as yet unidentified machinery. In addition, there are a number of transient signals: based on waveform analysis compared to a known car signal (Supplemental Figs S10, S11) and correlation with the CGN air traffic schedule, signals with dominant energy between 10 and 30 Hz can be related to passing cars, whereas transient events that have their main energy at higher frequencies, i.e. above 30 Hz, can be related to airborne traffic. This includes either the interaction between the airplane and both the ground and the air during starting and landing at close-by CGN airport, or signals generated during the close fly-by of airplanes and helicopters that show a characteristic Doppler shift in the spectrogram (Eibl et al., 2015; Meng and Ben-Zion, 2018; Díaz et al., 2022). In addition to cars for personal transport of employees, there is heavier traffic on the campus, e.g., due to trucks related to construction, but there is also a regular shuttle bus connecting the neighboring air force barracks with the Institute of Aerospace Medicine on campus. This bus passes along the roughly east-west oriented road in front of the MUSC building, but turns before reaching the location of LUNA. In this way, it acted as a repeatable source during the long-term recordings.

More exotic transient sources like the wind tunnel exist as well. As this source is only active in specific short time intervals that happen less than once a week, it has not yet been recorded at the location of LUNA. Supplemental Fig. S10c gives an example of the wind tunnel signal recorded during the long-term installation. The signal lasts about 12 s, has a clear start and end, and contains energy from 4 Hz all the way up to more than 90

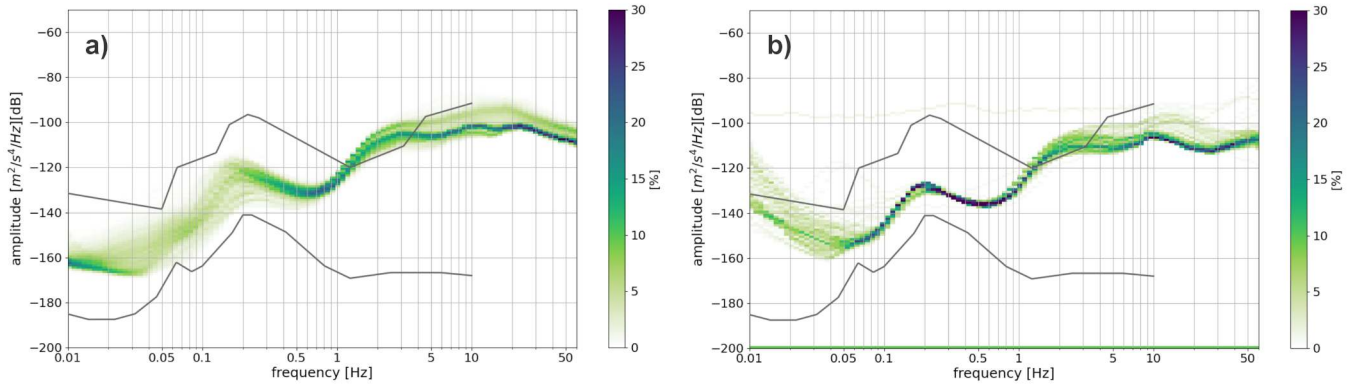

Figure 3 (a) Vertical-component PPSD for the long-term recording in the MUSC building. Data spans 51 continuous days in summer 2023 and 123 continuous days during the following winter and spring. Gray lines indicate Peterson's new low noise model and new high noise model (Peterson, 1993). (b) Vertical-component PPSD for the broad-band station at the center of the array at the future LUNA location, covering 3 days of data in August 2023.

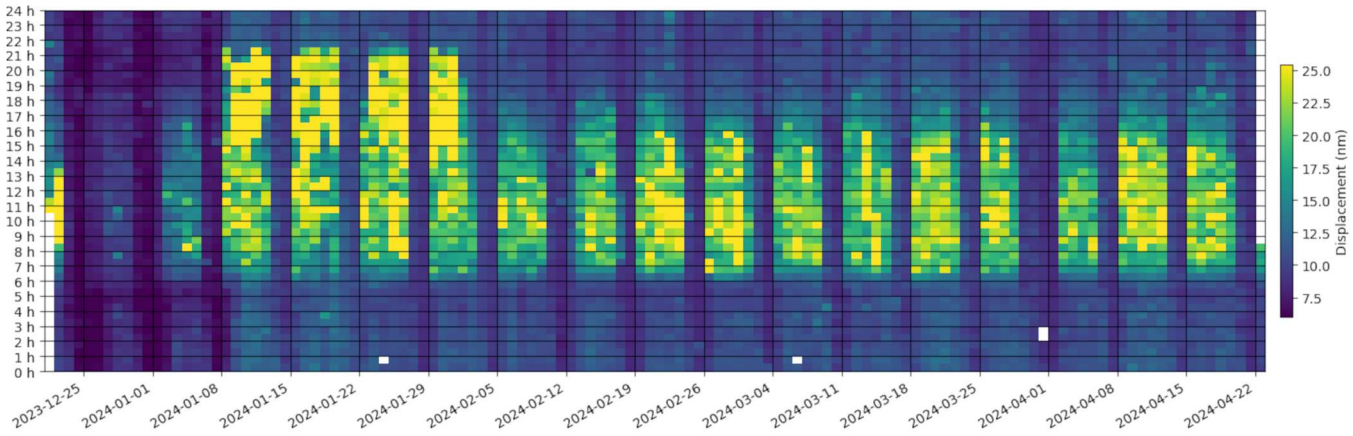

Figure 4 Changes in the vertical-component ambient displacement wavefield in the 4–20 Hz frequency band over time during 123 days of continuous recordings from December 2023 to April 2024. Time is in local time, and the one-hour gap between 2 and 3 am on March 31st is due to the change from daylight saving time to summer time. Code provided by Lecocq et al. (2020b) is used for the analysis.

Hz. This broad frequency content sets it apart from signals generated by traffic.

3.3.1 Cars

Signals from cars driving along the roughly east-west oriented road north of the array mainly cover the octave bands between 8 and 64 Hz (Fig. 5 and Supplemental Fig. S10a) and have a distinct shape in the seismograms (Fig. 6a). The closest distance to the road from the center of the array is about 50 m, which is well within the range of distances considered by Meng et al. (2021) when analyzing seismic signals of cars along dirt roads. Their car-generated signals have an emergent onset, no clear internal structure, and rise in amplitude to a maximum before symmetrically decreasing again, with rise and decay times both on the order of 10 s. Comparable signals, but with a shorter duration, are for example shown by Chai et al. (2025) and Hashima et al. (2025) for the passage of individual cars measured by stations directly next to a road, and used for traffic monitoring. In contrast, our recordings of cars contain a number of short bursts of energy, generally with two distinct amplitude maxima per burst, and no gradual increase or decrease in amplitude. Since the road in our case is a tarmac road which, over the length shown in Fig. 1, contains a number of irregularities like manholes, cracks, and bumps, and the recorded pattern is distinct, depending on whether a car is driving eastward or westward (Fig. 6a), we hypothesize that the signals we observe are generated at specific points on the road that present some irregularity (Czarny et al., 2023; Liu et al., 2025), rather than continuously all along the road, and that the two maxima are caused by the motion of the two axles of the car over the corresponding irregularity. The amplitude of the signal in this case not only depends on the distance from the array, but also on the size of the bump or crack.

This hypothesis is validated by a test using the array data to track a known car (Toyota Prius) along a predefined route, first driving out of the parking lot and from east to west along the road, then turning at around 368.25 E and driving back, entering a loop at the eastern end of the road near 368.53 E to turn again (Fig. 6), with a velocity approximately at the speed limit on campus of 30 km/h. We compared results from three different

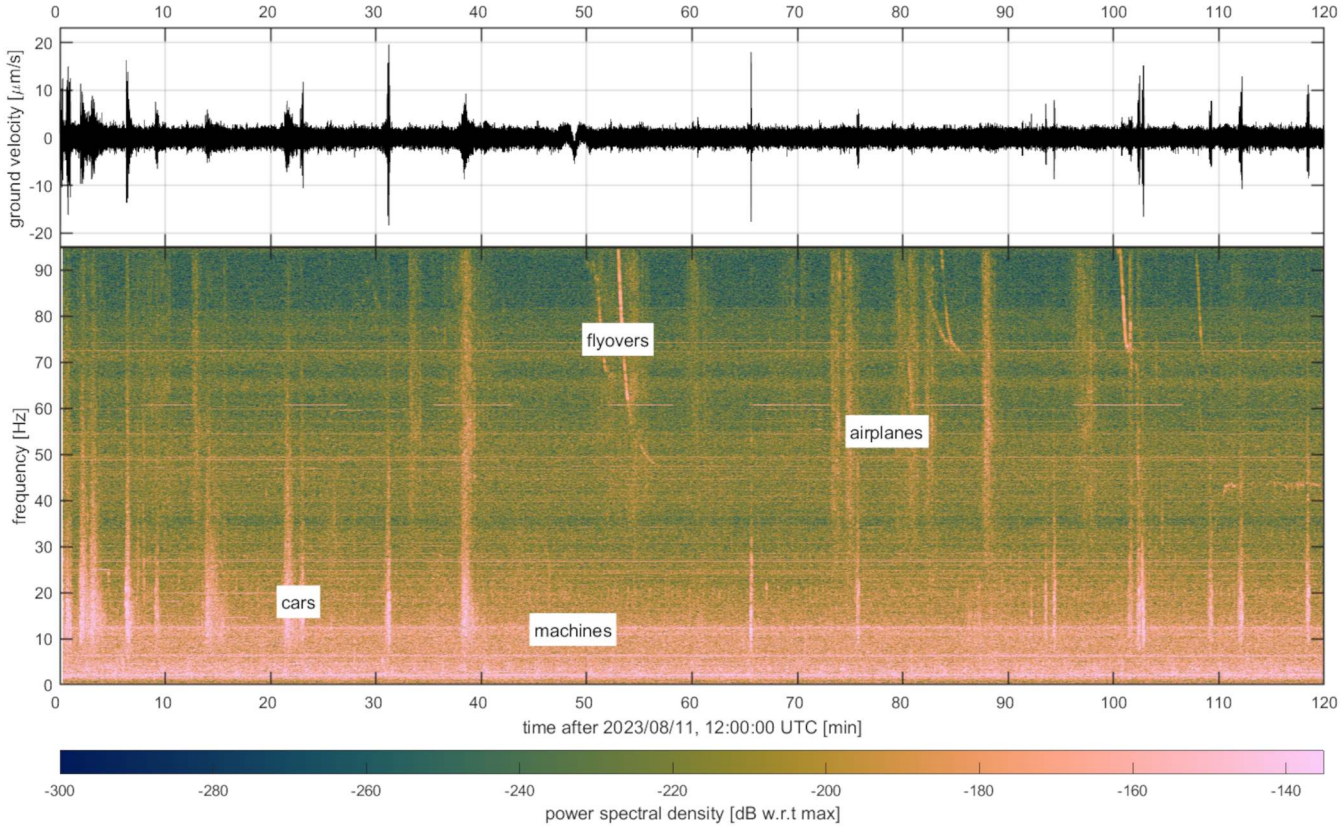

Figure 5 Vertical component seismogram and spectrogram covering two hours of daytime data on a weekday during the reference array measurement. Examples of typically observed noise sources are labeled.

methods to determine the backazimuth to the moving source, as each had some limitations in application to this dataset. In all cases, the seismograms were filtered between 5 and 30 Hz to clearly bring out the car-related signals.

Firstly, we applied array beamforming to the vertical component signals, using a 1^o grid in backazimuth and 230 equidistant samples across a slowness range from 1.2 to 10 s/km. To avoid issues with limited similarity between high-frequency waveforms at the different stations, we used waveform envelopes and calculated the sum of the cross-correlations between the envelope at the central station and the three other stations over a given time window. Examples for specific parts of the car signals are mapped in Fig. 6b–i, with the corresponding time windows indicated and labeled in Fig. 6a.

Secondly, we applied the hyperbola method for event location (Mohorovičić, 1915-1918) by picking the same signal phase at all four stations and minimizing the least squares misfit of the differential travel-times between arrivals at all sets of two stations, assuming a velocity of 280 m/s as previously derived for Rayleigh waves from the array analysis (Fig. 2a). Since the signal source lies well outside of the station network, distance is not well determined by this method, so we focus on the resulting azimuthal information. The two standard deviation range of the determined backazimuths is indicated by solid blue lines in Fig. 6b–i.

Finally, assuming the car-generated signals consist of Rayleigh waves, we used polarization information to determine the source direction. Rayleigh waves are elliptically polarized in the vertical-radial (Z-R) plane, with a phase shift of 90^o between the two components. We rotated the horizontal components of the central array station into tentative radial and transverse directions, using backazimuths between -90^o and 90^o with a 1^o increment, based on the known course of the road. We used the same time windows as in the beam forming (Fig. 6a) and calculated the cross-correlation coefficient between the Hilbert-transformed radial and the vertical component, which should show a maximum for the actual source angle. No Rayleigh wave energy should be projected on the transverse component, so we also calculated the cross-correlation coefficient between the Hilbert transform of the transverse component and the vertical, and maximized the ratio of the two cross-correlation coefficients in an absolute sense. This resulted in sharp maxima, marked by light-blue dashed lines in Fig. 6b–i. We compared with the results for source backazimuth determination by Rayleigh waves as described in Carrasco et al. (2023), which maximizes the energy on the vertical and radial components in a given time window as compared to the transverse. That method provided broader ranges of possible solutions, which always bracketed the solutions based on waveform cross-correlation as shown here.

The results obtained by all three methods are in broad agreement and show a consistent pattern following the trajectory of the car. This also demonstrates the fea-

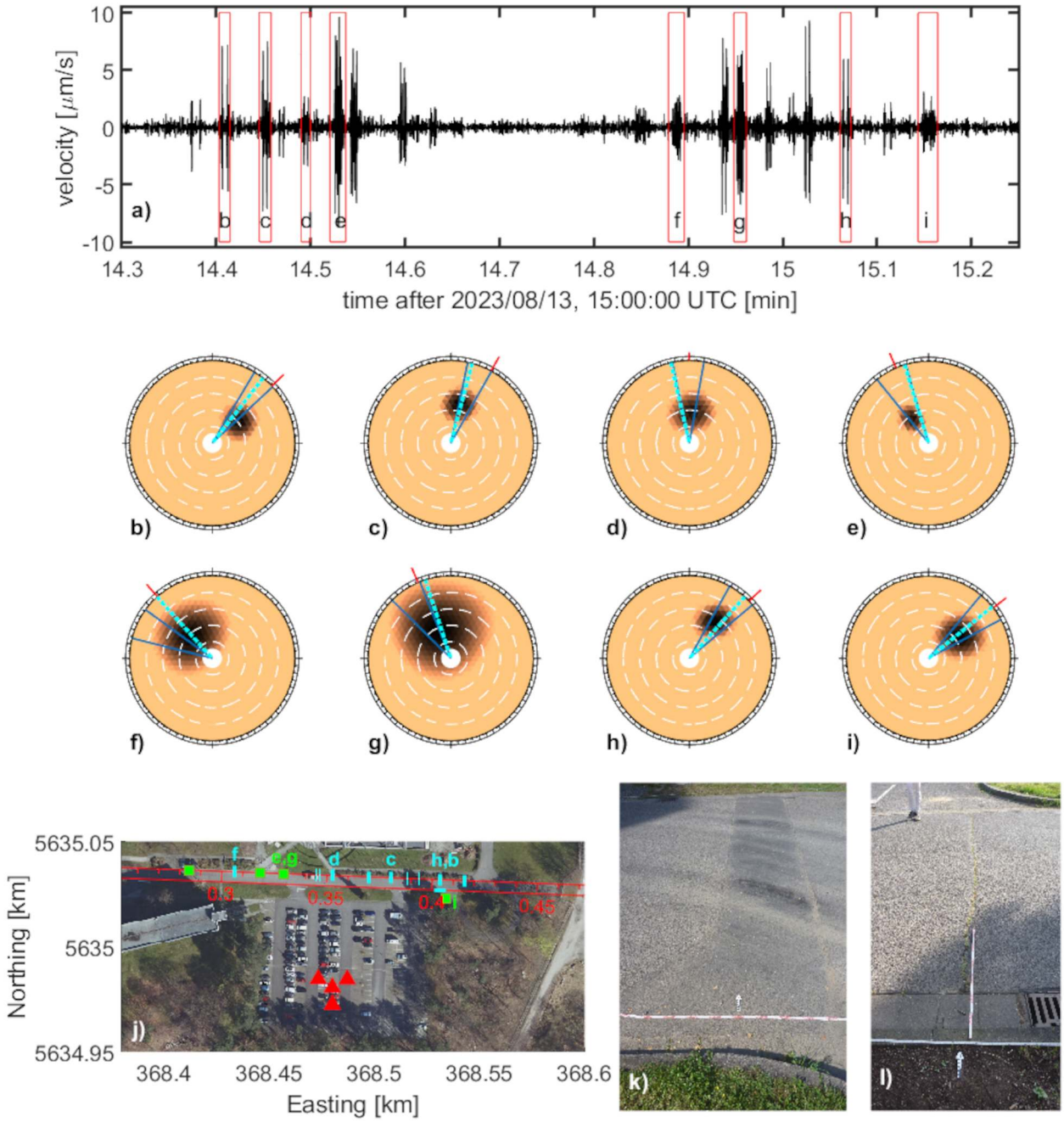

Figure 6 a) Vertical component seismic velocity data, registered at the center of the four-sensor array, for a Toyota Prius driving by the seismic array from east to west before turning and going back west to east and entering the turning loop at the end of the road. Time windows analyzed in subplots are marked in red and labeled. b)–i) Summary of analyzing the corresponding time windows. Colored background pattern indicates results of array beamforming, with amplitudes within 97% of the maximum beam power in darker colors. White dashed circles mark slowness values of 2, 4, 6 and 8 s/km, respectively. Solid blue lines indicate two standard deviations of the backazimuth determined with the hyperbola method, whereas dashed cyan line indicates azimuth determined from Rayleigh wave polarization. Red marker outside the azimuth ring indicated actual direction to mapped road damage associated with the seismic signal. j) Map of array location (red triangles), the road (read lines with distance markings in km), cracks mapped in the road (cyan lines), and broader craggedness (green squares). Thin lines mark small, narrow cracks not correlated with any signal in the seismic data. Irregularities associated with any of the signals analyzed above are marked by corresponding letters. Orthoimage as in Fig. 1. k) Example of broader bumpiness in the road, linked to more complex seismic signals, in this case e and g. l) Example of crack in the road, linked to a clearer pattern of the two car axles, in this case signal c.

sibility of tracking a car along the road with a single station, as opposed to an array of sensors (e.g. Riahi and Gerstoft, 2015; Díaz et al., 2022; Sheng, 2023) or roadside DAS (e.g. Wang et al., 2020, 2022), based on Rayleigh wave polarization. Some differences between the results from the three methods can be expected, as the first and third method use the waveform within the indicated time windows, while the second method is

based on the timing of a distinct phase within that window. The small number of stations limits the resolution of both the beamforming and the hyperbola method. On the other hand, the single-station method based on Rayleigh wave polarization assumes that Rayleigh waves are indeed dominant in the considered time windows. Deviations from a 90^o phase shift between the vertical and radial component of Rayleigh waves has previously been observed in field data (Carrasco et al., 2023, and discussion therein), so it might occur. The best-fit slownesses derived from beamforming lie between 3.6 and 5 s/km, translating to velocities between 200 and 280 m/s, in agreement with surface wave velocities. Similar waveform patterns, i.e. those in windows b and h, and those in windows e and g, show, within the measurement uncertainties, identical source backazimuths. This is in keeping with individual, rough patches of road acting as sources, and, based on the azimuthal information, we tried to locate those patches.

We mapped bumps, cracks, and manholes in the road from its eastern end to about 300 m west of the array center. Considering the derived backazimuths, signals are generated about 60 m up and down the road from the point of closest approach to the array. We also noted that there are differences in the waveforms of the signals, between, e.g., signal b (and h), that consists of two clear wiggles only, and signal e (and g), which is more complex. We take this as an indication that the signals are either generated by a single crack (Fig. 6l), or by a more complex piece of roadwork (Fig. 6k). Together with the backazimuth information, this allows correlating the signals with the mapped irregularities in the road (Fig. 6j), including signals for which the backazimuth analysis is not shown. Measured backazimuths from the center of the array to the corresponding mapped rough road patches are indicated by red lines in Fig. 6b–i. With the exception of the direction determined by the hyperbola method in case f, the backazimuths to the mapped craggedness show excellent agreement with the seismically determined source directions. As signal f shows a comparatively complex shape, the identification of equivalent phases at the four array stations is more difficult than in the case of signals with clear maxima, and the backazimuth derived by the hyperbola method might be affected by this.

Based on the measured locations of the sources on the road and the arrival time differences of the generated signals, we can determine the speed of the car. Since the difference in the distance between adjacent signal-generating cracks and bumps on the road and the array center is less than 10% of the total distance, and the Rayleigh wave velocity is significantly higher than the velocity of the car, we can neglect the contribution of the difference in ray path from adjacent obstacles to the array to the arrival time difference. The resulting car speeds are between 45 km/h and 14 km/h, with the highest velocities in the center of the stretch of road driven, and lower velocities near the ends, close to the turning points. These velocity estimates also agree with independent estimates based on measuring the time difference between the two main maxima for crack-generated signals and using the distance between the two axles of a Toyota Prius (2.7 m) to determine the velocity when crossing specific irregularities. The average velocity along the whole stretch of road between the cracks generating signal f on the one hand and signals h and b on the other hand, which have a distance of 98 m from one another, is in good agreement driving in both directions, at 31 km/h going east to west and 33 km/h going west to east. The identification of the specific patches of road that generate the observed seismic signals, via comparing the seismic data for a known course of the car and a map of the road, thus allows monitoring the driving-direction and speed of passing vehicles with a single station (Supplemental Section S3 and Supplemental Fig. S11).

3.3.2 Bus

The bus signal has some similarities to the car signal, in that it contains several sharp amplitude maxima and energy at high frequencies above 20 Hz (Supplemental Fig. S10b). The correspondence between parts of the signal and individual axles of the vehicle is less clear here. Besides, the passing bus generates an additional signal that is related to ground tilt and most clearly apparent in the 0.063–0.125 Hz octave band (Supplemental Fig. S10b, Fig. 7d–f). The timing of this signal does not coincide with the maximum amplitudes of the Rayleigh wave, and, when considering all three components (Fig. 7), shows similarity to seismic recordings of convective vortices, sometimes associated with dust devils, on Earth and Mars (Lorenz et al., 2015; Murdoch et al., 2021). The low-frequency tilt signal of terrestrial convective vortices has been obtained in the 0.01–0.1 Hz frequency band, with amplitudes as much as 10 times higher than those of the bus signals we observe (Lorenz et al., 2015, Figs 3, 6), whereas observations from Mars were done between 0.05 and 0.3 Hz and show comparable or lower amplitudes than those observed here (Lognonné et al., 2020; Garcia et al., 2020; Charalambous et al., 2021; Murdoch et al., 2021). These vortex signals have been successfully modeled as straight-line constant-speed migration of a negative point load on an elastic halfspace, where the pressure drop in the vortex pulls up the ground, with the effect of a typical-size dust devil compared to that of a small car (Lorenz et al., 2015). The car would act as a positive point load, depressing the ground and causing the ground to tilt towards the load. Low-frequency energy due to the quasi-static deformation caused by the weight of a passing car (Jousset et al., 2018; Lindsey et al., 2020; Yuan et al., 2020), as well as heavier vehicles (Wang et al., 2020), has indeed been observed in road-side DAS data.

The ground deformation caused by the bus can be approximated in terms of static deformation, expressed by the Boussinesq point load solution (Boussinesq, 1885). As the distance between the feet of the seismometer, on the order of 7 cm, is much smaller than the thickness of the uppermost layer of the subsurface (see Fig. 2), the subsurface can be approximated by a halfspace. As the velocity of the bus is much smaller than the Rayleigh wave propagation velocity, and the seismic wavelength at velocities above 400 m/s and for periods between 10

and 50 s is more than 100 times larger than the minimum distance between the road and the seismometer at about 25 m, the assumption of static deformation is reasonable. Fitting the recorded data is easiest done in terms of acceleration, since there are two contributions to the observed signal (Murdoch et al., 2017): acceleration due to direct vertical deformation of the ground, which is the only contribution on the vertical component; and acceleration due to differential vertical displacement of the seismometer feet, leading to an inclination against the normal in the gravity field, which is the main contribution on the horizontal components at low frequencies. In contrast to the single horizontal component obtained by DAS recordings, we can jointly invert all three components of acceleration, which have different dependencies on the free parameters.

The displacement response u_i to a vertical force F_3 according to Boussinesq (1885) is given by

$$u_i = \frac{F_3}{4\pi\mu}\left[\frac{x_3 x_i}{r^3} + (3-4\nu)\frac{\delta_{i3}}{r} - \frac{1-2\nu}{r+x_3}\left(\delta_{3i} + \frac{x_i}{r}\right)\right] \quad (3)$$

with the halfspace shear modulus μ and Poisson's ratio ν, the source-receiver distance $r = \sqrt{x_1^2 + x_2^2 + x_3^2}$, and δ the Kronecker symbol. Here, u_1 is the north component of displacement, u_2 the east component, and u_3 the vertical component.

The displacement is linearly related to the weight of the vehicle, but falls off as $1/r^2$ with the distance between vehicle and sensor (eq. 3). The bus is 4-5 times heavier than the cars considered in previous studies, but also further away, with a minimum distance of 25 m between seismometer and road, whereas the distance between fiber and road was as low as 2.5 m in previous studies (Lindsey et al., 2020). Besides, DAS records strain rate rather than velocity, which makes it more sensitive to quasi-static deformation than a seismometer. This might explain why the bus is more easily identifiable in our setup than individual passenger cars. Besides, the car-generated signals were most prominently observed at higher frequencies in strain, between 0.1 and 1 Hz (Jousset et al., 2018; Lindsey et al., 2020), which would make them more susceptible to damping as well as more prone to masking by the man-made noise on the campus (Fig. 3).

For small tilts, the acceleration due to tilt on the two horizontal components can be approximated by considering the differential vertical displacements at the three feet of the seismometer and their positions (Murdoch et al., 2017). For a Nanometrics Trillium compact, the diameter of the circle through the three feet is 82.3 mm according to the manufacturer. The feet form an equilateral triangle, with two feet on a north-south line and the third one to the east of this line. Starting in the north and moving clockwise when numbering the feet as $f1$ to $f3$, the acceleration in north direction $\ddot{u}_1$ and the acceleration in east direction $\ddot{u}_2$ due to the bus moving to the south of the seismometer can be approximated by

$$\ddot{u}_1 = g\frac{u_3^{f1} - u_3^{f3}}{x_1^{f3} - x_1^{f1}} \quad (4)$$

$$\ddot{u}_2 = g\frac{u_3^{f2} - (u_3^{f3} + u_3^{f1})/2}{x_2^{f1} - x_2^{f2}} \quad (5)$$

Assuming a mass m of the bus of 12000 kg, the vertical force exerted by the bus can be determined as $F = mg$. We model four vertical point forces, one at each wheel-road contact point (Jousset et al., 2018; Lindsey et al., 2020; Yuan et al., 2020), by assuming a distance of 6 m between the front and rear wheels of the bus, and 2.2 m between the left and right wheels. Note that the selected parameters are reasonable for a two-axle overland bus, but that various makes of bus were used for the transfer of military personal, and we do not have information on which type(s) of buses were in service on the specific day we selected for analysis here, or on the number of passengers during each trip, though from observation, this number was usually rather low. Free parameters in the calculation are then the velocity of the bus v_b that influences the source-receiver distance over time, μ, and ν. Whereas v_b influences both the amplitude and the shape of the observed signals, μ only affects the amplitude. The influence of ν is different depending on the component: on the vertical component, it only affects amplitude, whereas on the horizontals, it affects both shape and amplitude.

We perform a grid search for the inversion of the bus signals. We select eight signals that occurred during the 23rd of June 2023 with the expected signal shape for a vehicle passing from west to east along the road south of MUSC, at a regular cadence consistent with the observed passing of buses and an interval of approximately 30 min between buses. In addition, we chose clear signals with no discernible overlap with signals due to passing cars or an increased noise level in the primary microseismic band. Acceleration records are filtered between 10 and 50 s to clearly bring out the response to the load, and resampled to 20 sps to ease the computational burden. The date considered was a cloudy day in Cologne, with no rains within the time window considered, so we do not assume any changes in the subsurface elastic properties within this time frame. Differences between the different signals thus have to be related to the varying velocity of the bus v_b only, which could help to differentiate between the competing influence of ν and v_b on the acceleration response. We calculate the synthetic three-component acceleration for Poisson's ratio ν between 0.1 and 0.48 at an interval of 0.01, shear modulus μ between 80 and 1200 MPa in steps of 20 MPa, and velocity of the bus v_b between 15 and 40 km/h in intervals of 1 km/h, as the nominal speed limit on campus is 30 km/h. Synthetics are processed in the same way as the measured data, and we minimize the root-mean-squares (RMS) error between the measured and modeled data while giving a higher weight (0.4) to the vertical and east component and a lower weight (0.2) to the north component to prevent the higher amplitudes on the north component from dominating the misfit (Fig. 7d-f).

For each combination of values for ν and μ, we first independently minimize the misfit for each of the eight signals in dependence on the vehicle velocity. Resulting velocities for the bus are at the higher end of the inves-

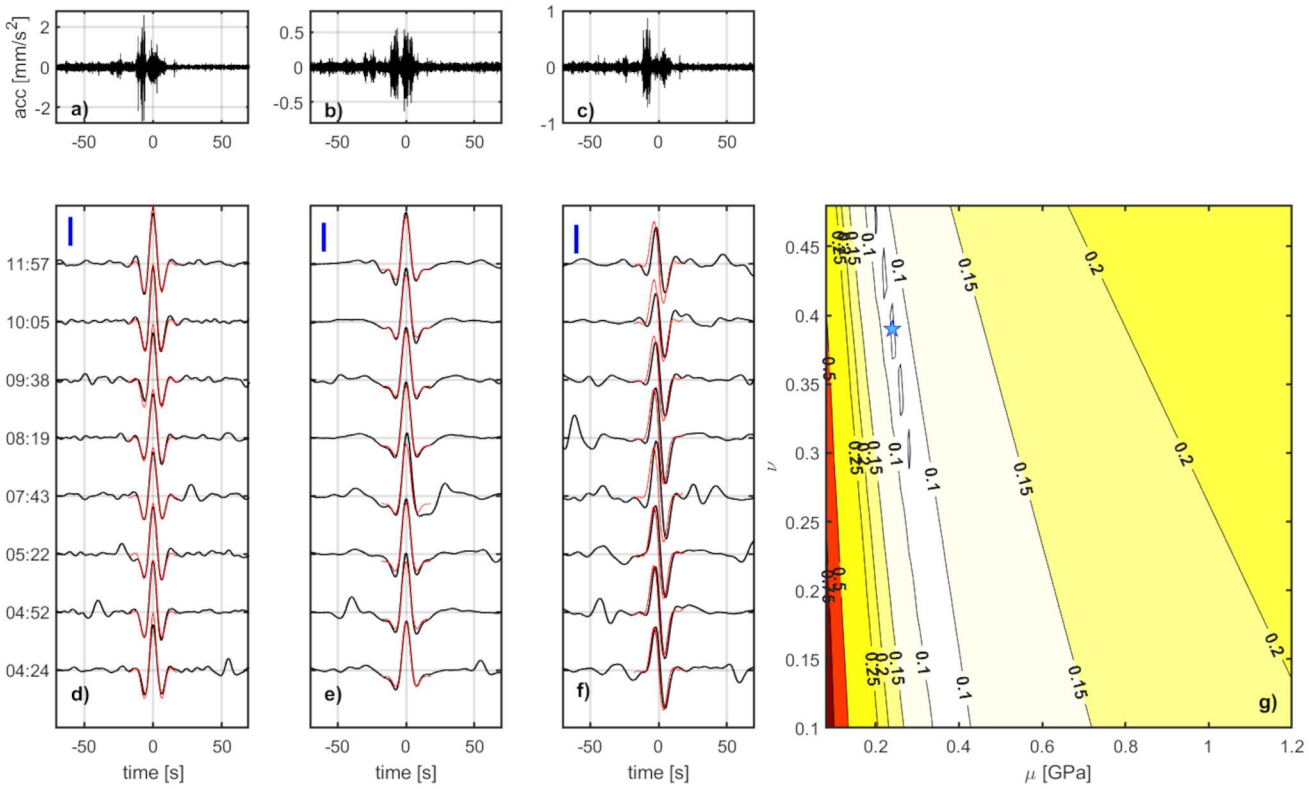

Figure 7 Modeling the quasi-static displacement in response to a passing bus. Examples of unfiltered acceleration records are given in a)–c) for the vertical, north, and east component, respectively. d)–f) show eight recorded bus signals (black solid lines) on the three components after filtering between 10 and 50 s and resampling to 20 sps, in comparison to the inverted data (red solid lines). The length of the blue scale bar is in d) 50 nm/s^2, in e) 250 nm/s^2, and in f) 150 nm/s^2. Labels on the left give the approximate timing of bus passage in UTC. The top-most signals are the same as shown in a)–c). g) Normalized misfit when simultaneously fitting all eight bus recordings. The minimum misfit is indicated by the blue star, and corresponds to the red lines shown in d)–f).

tigated parameter space, between 30 km/h for the signals at 07:43 and 08:19 UTC, and 40 km/h for the signals at 10:05 and 11:57 UTC. Lower velocities earlier in the morning might coincide with a larger amount of traffic, both vehicular and pedestrian, due to people arriving for work. The absolute minimum of the misfit is reached for a Poisson's ratio ν of 0.39 and a shear modulus μ of 240 MPa, but there is a significant trade-off and high uncertainty especially in ν (Fig. 7g). This might be avoided by tighter constraints on the actual velocity of the bus. Additional options include inverting for a combination of both elastic parameters (Murdoch et al., 2021), trying to separate them by just concentrating on the shape of the curve and ignoring the amplitude information (Yuan et al., 2020), or assuming a fixed value for one of them (Jousset et al., 2018).

The resulting values for elastic parameters are in the range expected for shallow sediments. A direct comparison to the velocity models derived for the LUNA location (Fig. 2d, e) is complicated by the fact that the building in which the seismometer was installed is offset vertically from the road by about 1 m via a step in the ground surface, both road and building have specifically constructed foundations, and might suffer from the simplifying assumption of a homogeneous half-space in the model. The difficulties due to the measurement setup could be avoided in future attempts at regolith characterization based on quasi-static deformation caused by passing rovers in LUNA, and on the Moon itself.

3.3.3 Airplanes and helicopters

The airplane-generated signals mainly visible at frequencies above 40 Hz can be linked to the take-off and landing of planes at CGN and might include engine-generated noise (both on the ground and in the air) as well as signals generated by the interaction between the aircraft's tires and the runway. The airport has three runways and serves all kinds of aircraft, from Boeing 747 cargo planes to executive jets, 24 hours a day. The closest distance from the array to any runway is less than 1 km, while the closest distance to the intercontinental runway, at 3815 m the longest runway at CGN, is about 2 km. The unique attribution of airplane signals to a specific departure or arrival listed on a website (Topsonic Systemhaus GmbH, 2022) provided as service by the airport, mainly for acoustic noise control, is at times impeded by the high cadence of airplanes, with up to 33 planes per hour, especially during the night time when CGN acts as an important transport hub for

air cargo. The time windows shown in Fig. 8 were selected so that within the 4 minutes shown, there was no overlap with any other airplane landing or taking off, since the timing provided by Topsonic Systemhaus GmbH (2022) does not always exactly match the start of the observed signal. Take-offs are consistently characterized by longer signals of the order of 60-80 s duration, while landings exhibit shorter signals of about 20 s duration with lower amplitudes, often with an impulsive start (Fig. 8). While the take-off signal could include sonic waves generated by the engines during acceleration, the landing signal could be explained by the initial touch-down, followed by friction between tarmac and tires coupling the airplane motion into the ground during braking. This would also explain the significantly longer signal duration compared to that recorded by DAS for an aircraft landing on the Northeast Greenland Ice Stream at a similar distance (Fichtner et al., 2023), where the interaction between ice and sled would produce less friction.

During the time period of 1.75 days analyzed in detail, over 630 take-offs and landings occurred (Topsonic Systemhaus GmbH, 2022), almost 550 of which—including those shown in Fig. 8—took place on the intercontinental runway, that is most likely to be used by larger aircraft. Within this data set, more than 60% of take-offs produced a clearly detectable signal, but less than 20% of the landings. This is in contrast to Riahi and Gerstoft (2015), who found signals from a comparable number of departures and arrivals in their data recorded close to an airport runway. However, their study was based on tracking the aircraft motion along a dense net of 74 receivers within 105 m of the runway, i.e. at a much closer distance, and did not report on the shape of individual signals or any differences between signals generated by take-offs and landings. Additional variations in signals might be linked to aircraft type, runway used, wind speed, or even pilot, but a more detailed analysis would require a larger data set (e.g., including different wind conditions and more traffic on the other two runways) and lies beyond the scope of this study.

In addition to airplane-ground interactions during take-off and landing, signals from airborne planes and helicopters were recorded as well (Fig. 9). Compared to signals generated by airplane-ground interaction, recordings of air traffic are rare—take-offs or landings are generally not associated with signals that show the flyby of the same aircraft. Previous studies of airplane signals used recordings tens of kilometers away from the nearest airport (Meng and Ben-Zion, 2018; Schippkus et al., 2020; Díaz et al., 2022), while our data were recorded much closer to the runways. The proximity to the airport could mean that planes are usually not flying at a constant velocity, and along a straight line, when within the range of our sensors, and accordingly do not generate the clear Doppler-shifted signals in spectrograms, spanning several minutes, that are characteristic of the radiation from a moving airborne source (Fig. 9). The future permanent station in LUNA will allow for more detailed studies of aircraft-related signals in close proximity to an airport.

The signals of near flybys by airplanes cover frequencies above 50 Hz, and extend beyond the frequency range covered by our sampling frequency of 200 Hz. They show a single Doppler-shifted energy band that starts at high frequencies and, over several minutes, tapers down to lower frequencies (Fig. 9b). In contrast, the blades of the main and tail rotor of a helicopter generate a number of harmonics in the seismic signal, occurring at multiples of the blade passing frequency. This is apparent in the signal shown in Fig. 9e, and the fundamental frequency around 27 Hz is similar to that observed in other studies (Eibl et al., 2017; Díaz et al., 2022).

As shown by Eibl et al. (2015), the time-frequency characteristics of air traffic events can be modeled by

$$f(t) = \frac{c \cdot f_s}{c + \frac{v_s^2 \cdot (t - t_0)}{\sqrt{v_s^2 \cdot (t-t_0)^2 + l^2}}} \tag{6}$$

where t_0 is the timing of the closest approach at distance l, f_s is the acoustic source frequency, v_s is the radial velocity of the source, and c is the velocity of sound in air, set to 331.45 m/s (Rienstra and Hirschberg, 2004). We extracted $f(t)$ from short-term Fourier transforms over 2 s long time windows with 50% overlap between consecutive windows (Figs 9c, f) and fitted the curves by performing a grid search over t_0, f_s, v_s and l and minimizing the RMS misfit.

For the airplane signal, some gaps in the curve result due to overlap with a simultaneously occurring landing listed at 12:54:20 UTC (Topsonic Systemhaus GmbH, 2022). The missing high-frequency end of the Doppler curve leads to some ambiguity in the resulting parameters: the optimum fit, as shown in Fig. 9c, is achieved for a closest approach of 14.62 km at t_0 = 83 s, for a source moving at a radial velocity of 730 km/h with an acoustic source frequency of 77 Hz. However, due to the missing information on the flattening of the Doppler curve at high frequencies, a good fit can still be obtained for lower distances of closest approach, down to 10 km, corresponding to t_0 = 90 s, v_s = 600 km/s, and f_s = 73 Hz. The frequency and velocity range is reasonable, given that we can only measure the radial component of the velocity: cruising speeds of passenger aircraft lie between 800 and 1000 km/h, and a frequency corresponding to 4500 RPM is in the range of the typical fan blade rotation of jet engines (Carney et al., 2009; Amoo, 2013).

For the helicopter signal, the curves for the three harmonics were fitted simultaneously, taking advantage of the fact that the frequencies of the harmonics are two and three times as large as the one of the fundamental mode. The best fit to the data results for a closest approach of 2245 $\pm$ 5 m at a t_0 = 132 $\pm$ 1 s, for a source moving at a radial velocity of 200 $\pm$ 1.4 km/h with an acoustic source frequency of 25.4 $\pm$ 0.2 Hz (Fig. 9f), pointing to a four-blade helicopter when taking into account typical RPMs (Eibl et al., 2015).

4 Summary and conclusions

In order to provide a broad scope of capabilities in supporting lunar instrument development and testing and procedures and operations training, the LUNA Moon

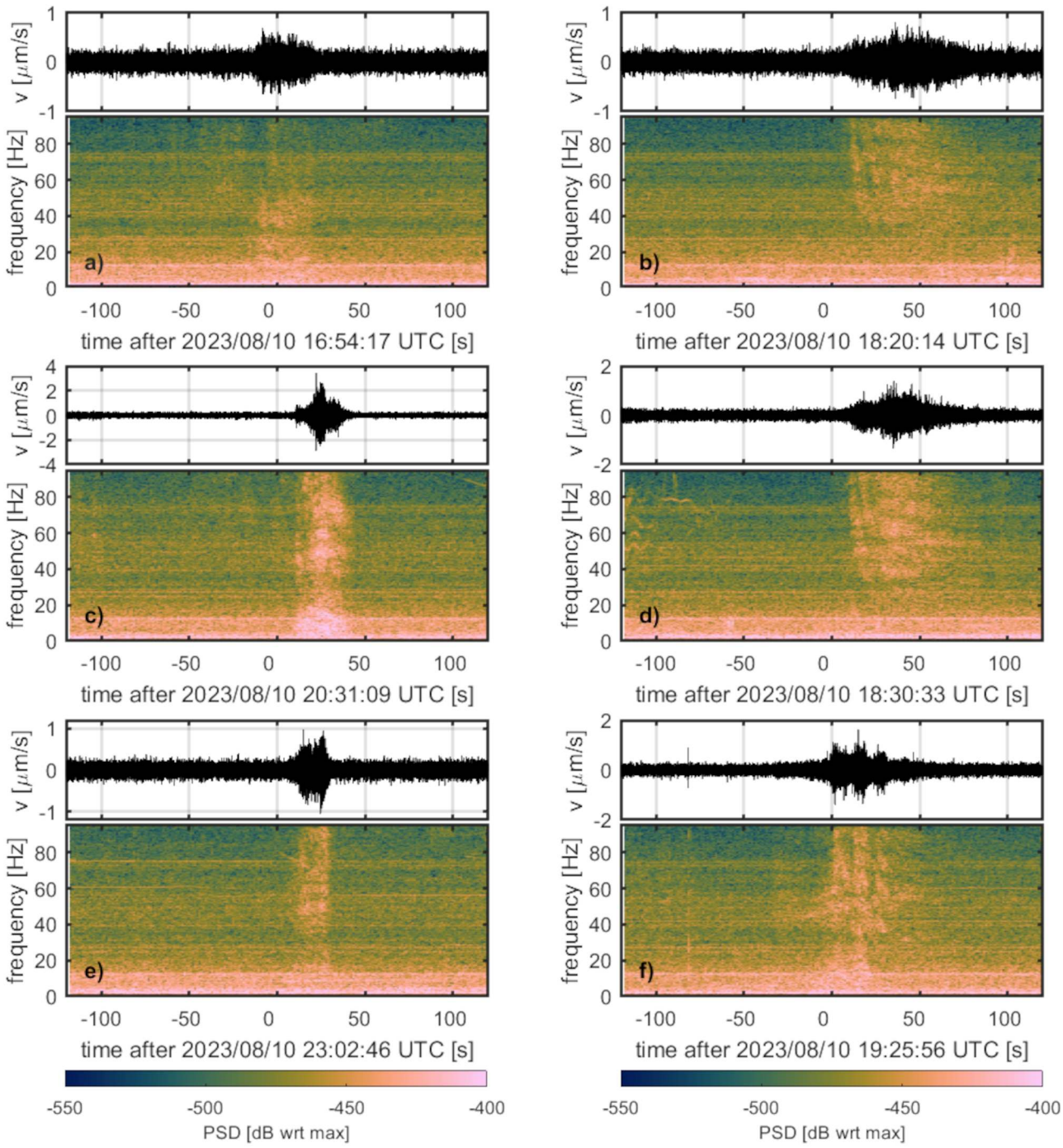

Figure 8 Examples of clearly visible airplane signals that could be uniquely associated to the timing of an arrival (left column) or a departure (right column) as listed by Topsonic Systemhaus GmbH (2022), used here as zero time. Shown are the vertical-component seismogram high-passed at 20 Hz and the corresponding, unfiltered spectrogram. (a), (c) Arrivals of UPS cargo flights. (e) Arrival of Sunexpress passenger flight (likely Boeing 737). (b) Departure of Ryanair passenger flight. (d) Departure of DHL cargo flight. (f) Departure of UPS cargo flight.

analogue facility will include a permanent broad-band seismic station as well as a buried fiber-optic cable. The siting of LUNA in an urban location means that anthropogenic noise will be an issue for seismic experiments or equipment testing for lunar applications conducted in the hall. Data on the background noise level and its temporal variability are hence important for the design and interpretation of these experiments. As the regolith layer within most of the hall is rather thin, future seismic experiments might also record reflections or refractions from strata below the hall, and might see the effect of the more than 150 m of sediments below LUNA. Accordingly, a good knowledge of the velocity structure below the site is required to interpret these signals. Information on signals commonly observed on the campus and their characteristics is important to allow for the correct attribution of signals recorded during seismic instrument tests in LUNA. Measurements

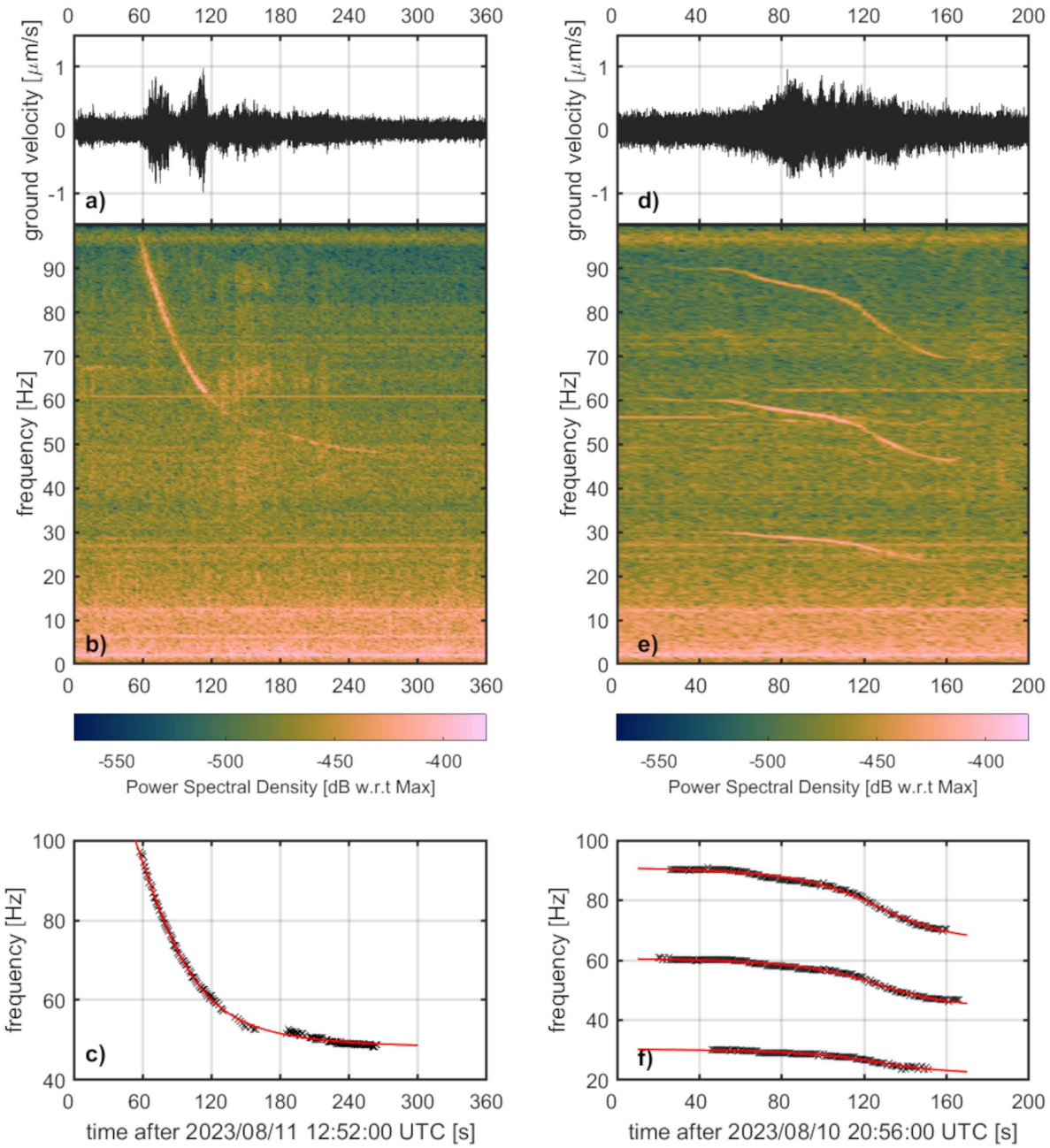

Figure 9 a) Vertical component velocity-proportional seismogram, high-passed at 40 Hz, of an airplane flyby recorded during the array measurement. b) Corresponding spectrogram. c) Doppler pattern extracted from the spectrogram (black crosses) and best fit based on equation 6 (red line). d) Vertical component velocity-proportional seismogram, high-passed at 20 Hz, of a helicopter flyby recorded during the array measurement. e) Corresponding spectrogram. f) Doppler patterns extracted from spectrogram (black crosses) and best fit for all three harmonics simultaneously, based on equation 6 (red lines).

in the undisturbed environment before the construction of the hall provide a reference for comparison to planned, similar measurements within the hall and allow for identifying any additional effects or new sources of noise due to e.g. the building itself. In addtion, our study shows how typical signals might be used to either characterise LUNA and its subsurface or for independent research like traffic monitoring.

The subsurface velocity structure at the LUNA location leads to site effects that are clearly visible e.g. in teleseismic recordings (Supplemental Fig. S8). We combined active and passive seismics and body and surface waves to characterize the site (e.g., Hobiger et al., 2021) and derive v_P and v_S models down to the bedrock. Particularly, refraction seismics and array measurements sensitive to shallow velocity structure provided a valuable complement to measurements of the ellipticity peak frequency. When applying equations reported in the literature for the LRE to directly derive bedrock depth from the HVSR peak frequency, the effect of lithology, as included in the relations by Budny (1984), turned out to be important. In particular, v_S below 80 m depth in our inversion-derived velocity models is compatible with velocity relations for clays, but

not for sands, which are more relevant for the western LRE, but have a dominant influence in some previously reported equations (Parolai et al., 2002). For our data from the DLR campus, a relation between HVSR peak frequency and bedrock depth recently proposed by Finger et al. (2025) that assumes an average v_S of 400 m/s, which is close to clay velocities across the whole 150 m of sediments in our models, provides a good fit to borehole information and the inverted model. It would accordingly be a good candidate for a HVSR based mapping of bedrock depth across the campus and beyond. Our inverted velocity models also show that, at the location of LUNA, the groundwater table has a more pronounced effect on shallow seismic velocities than the transition in lithology, as differences between sand and clay velocities mainly appear at larger depths.

The comparatively noisy environment of the permanent seismic station in LUNA will allow the long-term study of anthropogenic noise sources using broad-band data under unique conditions, i.e. car traffic on a private road, airborne traffic in the close vicinity of an airport, and machinery like wind tunnels. As discussed in the text, signals generated by cars and airplanes look distinct and different from what was previously reported in the literature (Meng et al., 2021; Fichtner et al., 2023; Chai et al., 2025; Hashima et al., 2025), indicating the variability of seismic responses under different environmental conditions. In the future, additional sources within the LUNA building, e.g. a heavy-lift crane, the gravity off-loading system, and the inflatable ramp can also be studied and characterized. Our results show that traffic signals could be used as repeating sources in LUNA, either of surface waves or quasi-static load, potentially allowing the study of temporal variations in subsurface properties like regolith compaction. The quasi-static load of passing rovers could potentially also be used for regolith characterization on the Moon. Beyond LUNA, our analysis indicated that monitoring the direction and speed of cars—at least in the somewhat controlled environment of the DLR campus—is possible with just a single seismometer. The clear identification of airplane signals, both from departures and landings at neighbouring CGN airport and due to overflights, means that the station could also be used for more detailed airtraffic studies (e.g. Seppi et al., 2025).

More generally, the permanent seismometer in LUNA will suffer from an increased noise level above 1 Hz due to anthropogenic activity in the vicinity, even while no activity is happening in LUNA itself. However, the long-period noise level appears more promising and will allow the use of the station in studies focusing on teleseismic data. Since even small local events can be detected under favorable conditions (Supplemental Section S2 and Supplemental Fig. S9), the station could occasionally also improve local monitoring, especially since current station coverage south of Cologne on the Eastern bank of the river Rhine is sparse (Stammler et al., 2021).

Acknowledgements

The authors and the entire LUNA project team want to acknowledge the government of North Rhine-Westphalia for the funds received to finance the outfitting of the LUNA facility.

We gratefully acknowledge the Institute of Geophysics and Meteorology at University of Cologne for providing instrumentation for the active seismic measurements. We thank Sebastian Carrasco, Michael Hartmann and Peter Mora from Bensberg Observatory, University of Cologne, for their aid in conducting those measurements.

We thank two anonymous reviewers for their detailed comments that helped to improve the manuscript.

Data and code availability

Seismic data from the refraction profile, array measurements, and test installation in the MUSC building as analyzed in this manuscript is available at Zenodo via Knapmeyer-Endrun et al. (2025) under a Creative Common Attribution 4.0 International license. Continuous miniSEED data from Bensberg Observatory used in Supplementary Fig. S8 is available at EIDA via Department of Geosciences, Bensberg Observatory, University of Cologne (2016).

Version 1.4.0 of ObsPy used to calculate and plot PPSD is preserved at Zenodo (The ObsPy Development Team, 2022). Version 1.0 of SeismoRMS used in the analysis of temporal variations in the seismic noise is preserved at Zenodo (Lecocq et al., 2020b). Version 2.0 of MASWaves used for MASW analysis is preserved at https://uni.hi.is/eao4/. Version 2.0 of RayDec used for ellipticity measurements is preserved at Zenodo (Hobiger, 2021). Version 3.3.3 of Geopsy and version 1.1.2 of dinver (3.4.2-preview), used for ambient vibration analysis and inversion, is preserved at https://www.geopsy.org and available under GNU Public License v3. The perceptually uniform Batlow colormap (Crameri et al., 2020) used in Figs 5, 8 and 9 is preserved at Zenodo (Crameri, 2018).

Competing interests

The authors have no competing interests.

References

Aboobaker, A., Panning, M., and Bugby, D. The Farside Seismic Suite: A novel approach for long-term lunar seismology. In *2024 IEEE Aerospace Conference*, pages 1–8, 2024. doi: 10.1109/AERO58975.2024.10521223.

Aki, K. Space and time spectra of stationary stochastic waves, with special reference to microtremors. *Bulletin of the Earthquake Research Institute*, 35:415–456, 1957.

Amoo, L. M. On the design and structural analysis of jet engine fan blade structures. *Progress in Aerospace Sciences*, 60:1–11, 2013. doi: 10.1016/j.paerosci.2012.08.002.

Bonnefoy-Claudet, S., Cornou, C., Bard, P.-Y., Cotton, F., Moczo, P., Kristek, J., and Fäh, D. H/V ratio: a tool for site effects evaluation. Results from 1-D noise simulations. *Geophysical Journal International*, 167(2):827–837, 2006. doi: 10.1111/j.1365-246X.2006.03154.x.

Bonnefoy-Claudet, S., Köhler, A., Cornou, C., Wathelet, M., and Bard, P.-Y. Effects of Love waves on microtremor H/V ratio.

Bulletin of the Seismological Society of America, 98(1):288–300, 2008. doi: 10.1785/0120070063.

Boussinesq, M. J. *Application des Potentiels. A l'Étude de l'Équilibre et du Mouvement des Solides Élastiques*. Gauthier-Villars, Paris, 1885.

Budny, M. *Seismische Bestimmung der bodendynamischen Kennwerte von oberflächennahen Schichten in Erdbebengebieten der Niederrheinischen Bucht und ihre ingenieurseismologische Anwendung*. Phd thesis, University of Cologne, 1984.

Carney, K., Pereira, J. M., Revilock, D., and Matheny, P. Jet engine fan blade containment using an alternate geometry. *International Journal of Impact Engineering*, 36(5):720–728, 2009. doi: 10.1016/j.ijimpeng.2008.10.002.

Carrasco, S., Knapmeyer-Endrun, B., Margerin, L., Xu, Z., Joshi, R., Schimmel, M., Stutzmann, E., Charalambous, C., Lognonné, P., and Banerdt, W. B. Constraints for the martian crustal structure from Rayleigh waves ellipticity of large seismic events. *Geophysical Research Letters*, 50(16):e2023GL104816, 2023. doi: 10.1029/2023GL104816.

Casini, A. E., Mittler, P., Cowley, A., Schlüter, L., Faber, M., Fischer, B., von der Wiesche, M., and Maurer, M. Lunar analogue facilities development at EAC: the LUNA project. *Journal of Space Safety Engineering*, 7(4):510–518, 2020. doi: 10.1016/j.jsse.2020.05.002.

Chai, C., Marcillo, O., Maceira, M., Kerekes, R., and Canion, B. Identifying Vehicle Signals in Continuous Seismic Data Using Unsupervised Machine-Learning Techniques. *Seismological Research Letters*, 2025. doi: 10.1785/0220250202.

Charalambous, C., McClean, J. B., Baker, M., Pike, W. T., Golombek, M., Lemmon, M., Ansan, V., Perrin, C., Spiga, A., Lorenz, R. D., Banks, M. E., Murdoch, N., Rodriguez, S., Weitz, C. M., Grant, J. A., Warner, N. H., Garvin, J., Daubar, I. J., Hauber, E., Stott, A. E., Johnson, C. L., Mittelholz, A., Warren, T., Navarro, S., Sotomayor, L. M., Maki, J., Lucas, A., Banfield, D., Newman, C., Viúdez-Moreiras, D., Pla-García, J., Lognonné, P., and Banerdt, W. B. Vortex-Dominated Aeolian Activity at InSight's Landing Site, Part 1: Multi-Instrument Observations, Analysis, and Implications. *Journal of Geophysical Research: Planets*, 126(6): e2020JE006757, 2021. doi: 10.1029/2020JE006757.

Civilini, F., Weber, R., and Husker, A. Thermal moonquake characterization and cataloging using frequency-based algorithms and stochastic gradient descent. *Journal of Geophysical Research: Planets*, 128(9):e2022JE007704, 2023. doi: 10.1029/2022JE007704.

Crameri, F. Scientific colour maps [Software], 2018. doi: 10.5281/zenodo.1243862.

Crameri, F., Shephard, G. E., and Heron, P. J. The misuse of colour in science communication. *Nature Communications*, 11:5444, 2020. doi: 10.1038/s41467-020-19160-7.

Czarny, R., Zhu, T., and Shen, J. Spatiotemporal evaluation of Rayleigh surface wave estimated from roadside dark fiber DAS array and traffic noise. *Seismica*, 2(2), 2023. doi: 10.26443/seismica.v2i2.247.

de Paula, L. A. N., Norton, R. S., Paik, H. J., Schmerr, N. C., Williamson, P. R., Chui, T. C. P., and Hahn, I. High-sensitivity seismometer development for lunar applications. *Sensors*, 23(16), 2023. doi: 10.3390/s23167245.

Department of Geosciences, Bensberg Observatory, University of Cologne. Bensberg Earthquake Network [Dataset], 2016. doi: 10.7914/SN/BQ.

Díaz, J., Ruiz, M., Sánchez-Pastor, P. S., and Romero, P. Urban seismology: On the origin of Earth vibrations within a city. *Scientific reports*, 7(1):15296, 2017. doi: 10.1038/s41598-017-15499-y.

Díaz, J., DeFelipe, I., Ruiz, M., Andrés, J., Ayarza, P., and Carbonell, R. Identification of natural and anthropogenic signals in controlled source seismic experiments. *Scientific reports*, 12(1): 3171, 2022. doi: 10.1038/s41598-022-07028-3.

Eibl, E. P., Lokmer, I., Bean, C. J., Akerlie, E., and Vogfjörd, K. S. Helicopter vs. volcanic tremor: Characteristic features of seismic harmonic tremor on volcanoes. *Journal of Volcanology and Geothermal Research*, 304:108–117, 2015. doi: 10.1016/j.jvolgeores.2015.08.002.

Eibl, E. P., Lokmer, I., Bean, C. J., and Akerlie, E. Helicopter location and tracking using seismometer recordings. *Geophysical Journal International*, 209(2):901–908, 2017. doi: 10.1093/gji/ggx048.

Engelschiøn, V. S., Eriksson, S., Cowley, A., Fateri, M., Meurisse, A., Kueppers, U., and Sperl, M. EAC-1A: A novel large-volume lunar regolith simulant. *Scientific reports*, 10(1):5473, 2020. doi: 10.1038/s41598-020-62312-4.

Erwin, A., de Paula, L. A., Schmerr, N. C., Shelton, D., Hahn, I., Williamson, P. R., Paik, H. J., and Chui, T. C. Brownian noise and temperature sensitivity of long-period lunar seismometers. *Bulletin of the Seismological Society of America*, 111(6):3065–3075, 2021. doi: 10.1785/0120210072.

Essien, U., Akankpo, A., and Igboekwe, M. Poisson's ratio of surface soils and shallow sediments determined from seismic compressional and shear wave velocities. *International Journal of Geosciences*, 5(12):1540–1546, 2014. doi: 10.4236/ijg.2014.512125.

Fichtner, A., Hofstede, C., N. Kennett, B. L., Nymand, N. F., Lauritzen, M. L., Zigone, D., and Eisen, O. Fiber-optic airplane seismology on the Northeast Greenland Ice Stream. *The Seismic Record*, 3(2):125–133, 2023. doi: 10.1785/0320230004.

Finger, C., Keil, S., Gotowik, A., Jüstel, A., and Brotzer, A. Mapping sediment depths using seismic arrays, rotational measurements, and spectral ratios. *Acta Geophysica*, pages 1–11, 2025. doi: 10.1007/s11600-025-01552-2.

Garcia, R. F., Khan, A., Drilleau, M., Margerin, L., Kawamura, T., Sun, D., Wieczorek, M. A., Rivoldini, A., Nunn, C., Weber, R. C., et al. Lunar seismology: An update on interior structure models. *Space Science Reviews*, 215:1–47, 2019. doi: 10.1007/s11214-019-0613-y.

Garcia, R. F., Kenda, B., Kawamura, T., Spiga, A., Murdoch, N., Lognonné, P. H., Widmer-Schnidrig, R., Compaire, N., Orhand-Mainsant, G., Banfield, D., et al. Pressure effects on the SEIS-InSight instrument, improvement of seismic records, and characterization of long period atmospheric waves from ground displacements. *Journal of Geophysical Research: Planets*, 125(7): e2019JE006278, 2020. doi: 10.1029/2019JE006278.

Geologischer Dienst NRW. Bohrungen in NRW, 2023. https://www.bohrungen.nrw.de/. last accessed 2023/04/20.

Green, D. N., Bastow, I. D., Dashwood, B., and Nippress, S. E. Characterizing broadband seismic noise in Central London. *Seismological Research Letters*, 88(1):113–124, 2017. doi: 10.1785/0220160128.

Groos, J. and Ritter, J. Time domain classification and quantification of seismic noise in an urban environment. *Geophysical Journal International*, 179(2):1213–1231, 2009. doi: 10.1111/j.1365-246X.2009.04343.x.

Harmon, N., Porter, R., Rychert, C., Schmerr, N., Smith, M. M., Shen, Z., Wu, W., Giles, J., McCall, N., Wang, J., Wike, L., West, J., Hoyle, A., and Deykes, N. Distributed acoustic sensing for future planetary applications: Initial results from the San Francisco volcanic field, a lunar analogue. *Earth and Space Science*, 11(12): e2024EA003640, 2024. doi: 10.1029/2024EA003640.

Hashima, S., Saad, M. H., Ahmad, A. B., Tsuji, T., and Rizk, H. Effective deep learning aided vehicle classification approach us-

ing Seismic Data. *Scientific Reports*, 15(1):22624, 2025. doi: 10.1038/s41598-025-01684-x.

Hinzen, K.-G., Weber, B., and Scherbaum, F. On the resolution of H/V measurements to determine sediment thickness, a case study across a normal fault in the Lower Rhine Embayment, Germany. *Journal of Earthquake Engineering*, 8(06):909–926, 2004. doi: 10.1142/S136324690400178X.

Hobiger, M. RayDec 2.0 [Software], 2021. doi: 10.5281/zenodo.5534777.

Hobiger, M., Bard, P.-Y., Cornou, C., and Le Bihan, N. Single station determination of Rayleigh wave ellipticity by using the random decrement technique (RayDec). *Geophysical Research Letters*, 36(14), 2009. doi: 10.1029/2009GL038863.

Hobiger, M., Cornou, C., Wathelet, M., Giulio, G. D., Knapmeyer-Endrun, B., Renalier, F., Bard, P.-Y., Savvaidis, A., Hailemikael, S., Le, B. N., Ohrnberger, M., and Theodoulidis, N. Ground structure imaging by inversions of Rayleigh wave ellipticity: sensitivity analysis and application to European strong-motion sites. *Geophysical Journal International*, 192(1):207–229, 2012. doi: 10.1093/gji/ggs005.

Hobiger, M., Bergamo, P., Imperatori, W., Panzera, F., Marrios Lontsi, A., Perron, V., Michel, C., Burjánek, J., and Fäh, D. Site characterization of Swiss strong-motion stations: The benefit of advanced processing algorithms. *Bulletin of the Seismological Society of America*, 111(4):1713–1739, 2021. doi: 10.1785/0120200316.

Ibs-von Seht, M. and Wohlenberg, J. Microtremor measurements used to map thickness of soft sediments. *Bulletin of the Seismological Society of America*, 89(1):250–259, 1999. doi: 10.1785/BSSA0890010250.

Imazato, H., Ikeda, T., and Tsuji, T. Shallow S wave velocity profile from active source seismic data at the Apollo 14 landing site based on virtual multichannel analysis of surface waves. *Icarus*, 406:115724, 2023. doi: 10.1016/j.icarus.2023.115724.

John, J., Thamarai, V., Choudhary, T., Srinivasa, M., Jambhalikar, A., Giridhar, M., Mehra, M. M., Garg, M., Shila, K., Kummari, K., et al. Identification and preliminary characterisation of signals recorded by instrument for lunar seismic activity at the Chandrayaan 3 landing site. *Icarus*, 424:116285, 2024. doi: 10.1016/j.icarus.2024.116285.

Jousset, P., Reinsch, T., Ryberg, T., Blanck, H., Clarke, A., Aghayev, R., Hersir, G. P., Henninges, J., Weber, M., and Krawczyk, C. M. Dynamic strain determination using fibre-optic cables allows imaging of seismological and structural features. *Nature communications*, 9(1):2509, 2018. doi: 10.1038/s41467-018-04860-y.

Keil, S., Igel, H., Schimmel, M., Lindner, F., and Bernauer, F. Investigating subsurface properties of the shallow lunar crust using seismic interferometry on synthetic and recorded data. *Earth and Space Science*, 11(10):e2024EA003742, 2024. doi: 10.1029/2024EA003742.

Knapmeyer-Endrun, B., Golombek, M. P., and Ohrnberger, M. Rayleigh wave ellipticity modeling and inversion for shallow structure at the proposed InSight landing site in Elysium Planitia, Mars. *Space Science Reviews*, 211(1):339–382, 2017. doi: 10.1007/s11214-016-0300-1.

Knapmeyer-Endrun, B., Knapmeyer, M., Cornelius, O., Fischer, H.-H., Hallinger, M., Fantinati, C., Küchemann, O., and Maibaum, M. Seismic characterization of the subsurface and anthropogenic noise sources at the ESA-DLR LUNA Moon analogue facility [Data set], 2025. doi: 10.5281/zenodo.15113128.

Köhler, A., Ohrnberger, M., Scherbaum, F., Wathelet, M., and Cornou, C. Assessing the reliability of the modified three-component spatial autocorrelation technique. *Geophysical Journal International*, 168(2):779–796, 2007. doi: 10.1111/j.1365-246X.2006.03253.x.

Land NRW. ELWAS-WEB, 2023. https://www.elwasweb.nrw.de. last accessed 2023/05/03.

Lecocq, T., Hicks, S. P., Van Noten, K., Van Wijk, K., Koelemeijer, P., De Plaen, R. S., Massin, F., Hillers, G., Anthony, R. E., Apoloner, M.-T., et al. Global quieting of high-frequency seismic noise due to COVID-19 pandemic lockdown measures. *Science*, 369(6509): 1338–1343, 2020a. doi: 10.1126/science.abd2438.

Lecocq, T., Massin, F., Satriano, C., Vanstone, M., and Megies, T. SeismoRMS - A simple python/jupyter notebook package for studying seismic noise changes (1.0) [Software], 2020b. doi: 10.5281/zenodo.3820046.

Lindsey, N. J., Yuan, S., Lellouch, A., Gualtieri, L., Lecocq, T., and Biondi, B. City-scale dark fiber DAS measurements of infrastructure use during the COVID-19 pandemic. *Geophysical Research Letters*, 47(16):e2020GL089931, 2020. doi: 10.1029/2020GL089931.

Liu, X., Mi, B., Xia, J., Zhou, J., and Ma, Y. Deep clustering of traffic signals using a single seismic station. *Journal of Applied Geophysics*, 243:105979, 2025. doi: 10.1016/j.jappgeo.2025.105979.

Lognonné, P., Banerdt, W. B., Pike, W. T., Giardini, D., Christensen, U., Garcia, R. F., Kawamura, T., Kedar, S., Knapmeyer-Endrun, B., Margerin, L., et al. Constraints on the shallow elastic and anelastic structure of Mars from InSight seismic data. *Nature Geoscience*, 13(3):213–220, 2020. doi: 10.1038/s41561-020-0536-y.

Lorenz, R. D., Kedar, S., Murdoch, N., Lognonné, P., Kawamura, T., Mimoun, D., and Bruce Banerdt, W. Seismometer detection of dust devil vortices by ground tilt. *Bulletin of the Seismological Society of America*, 105(6):3015–3023, 11 2015. doi: 10.1785/0120150133.

Maranò, S., Hobiger, M., Bergamo, P., and Fäh, D. Analysis of Rayleigh waves with circular wavefront: a maximum likelihood approach. *Geophysical Journal International*, 210(3):1570–1580, 2017. doi: 10.1093/gji/ggx225.

Meng, H. and Ben-Zion, Y. Characteristics of airplanes and helicopters recorded by a dense seismic array near Anza California. *Journal of Geophysical Research: Solid Earth*, 123(6):4783–4797, 2018. doi: 10.1029/2017JB015240.

Meng, H., Ben-Zion, Y., and Johnson, C. W. Analysis of seismic signals generated by vehicle traffic with application to derivation of subsurface Q-values. *Seismological Research Letters*, 92(4): 2354–2363, 2021. doi: 10.1785/0220200457.

Mohorovičić, A. Die Bestimmung des Epizentrums eines Nahbebens. *Gerlands Beiträge zur Geophysik*, 14:199–205, 1915-1918.

Murdoch, N., Mimoun, D., Garcia, R. F., Rapin, W., Kawamura, T., Lognonné, P., Banfield, D., and Banerdt, W. B. Evaluating the wind-induced mechanical noise on the InSight seismometers. *Space Science Reviews*, 211:429–455, 2017. doi: 10.1007/s11214-016-0311-y.

Murdoch, N., Spiga, A., Lorenz, R., Garcia, R. F., Perrin, C., Widmer-Schnidrig, R., Rodriguez, S., Compaire, N., Warner, N. H., Mimoun, D., Banfield, D., Lognonné, P., and Banerdt, W. B. Constraining martian regolith and vortex parameters from combined seismic and meteorological measurements. *Journal of Geophysical Research: Planets*, 126(2):e2020JE006410, 2021. doi: 10.1029/2020JE006410.

Nakamura, Y. A method for dynamic characteristics estimation of subsurface using microtremor on the ground surface. *Railway Technical Research Institute, Quarterly Reports*, 30(1), 1989.

Nunn, C., Pike, W. T., Standley, I. M., Calcutt, S. B., Kedar, S., and Panning, M. P. Standing on Apollo's shoulders: A microseismometer for the Moon. *The Planetary Science Journal*, 2(1):36,

2021. doi: 10.3847/PSJ/abd63b.

Olafsdottir, E. A., Erlingsson, S., and Bessason, B. Tool for analysis of multichannel analysis of surface waves (MASW) field data and evaluation of shear wave velocity profiles of soils. *Canadian Geotechnical Journal*, 55(2):217–233, 2018. doi: 10.1139/cgj-2016-0302.

Onodera, K. New views of lunar seismicity brought by analysis of newly discovered moonquakes in Apollo short-period seismic data. *Journal of Geophysical Research: Planets*, 129(7): e2023JE008153, 2024. doi: 10.1029/2023JE008153.

Park, C. B., Miller, R. D., and Xia, J. Multichannel analysis of surface waves. *Geophysics*, 64(3):800–808, 1999. doi: 10.1190/1.1444590.

Parolai, S., Bormann, P., and Milkereit, C. New relationships between Vs, thickness of sediments, and resonance frequency calculated by the H/V ratio of seismic noise for the Cologne area (Germany). *Bulletin of the Seismological Society of America*, 92 (6):2521–2527, 2002. doi: 10.1785/0120010248.

Parolai, S., Richwalski, S. M., Milkereit, C., and Bormann, P. Assessment of the stability of H/V spectral ratios from ambient noise and comparison with earthquake data in the Cologne area (Germany). *Tectonophysics*, 390(1-4):57–73, 2004. doi: 10.1016/j.tecto.2004.03.02.

Peterson, J. R. Observations and modeling of seismic background noise. Technical Report Open-File Report 93-322, US Geological Survey, Albuquerque, New Mexico, 1993.

Riahi, N. and Gerstoft, P. The seismic traffic footprint: Tracking trains, aircraft, and cars seismically. *Geophysical Research Letters*, 42(8):2674–2681, 2015. doi: 10.1002/2015GL063558.

Rienstra, S. W. and Hirschberg, A. *Speed of Sound*, chapter 2.3. Technische Universiteit Eindhoven, 2004.

Salem, H. S. Poisson's ratio and the porosity of surface soils and shallow sediments, determined from seismic compressional and shear wave velocities. *Geotechnique*, 50:461–463, 2000. doi: 10.1680/geot.2000.50.4.461.

Sambridge, M. Geophysical inversion with a neighbourhood algorithm—I. Searching a parameter space. *Geophysical journal international*, 138(2):479–494, 1999. doi: 10.1046/j.1365-246X.1999.00876.x.

Schäfer, A., Utescher, T., Klett, M., and Valdivia-Manchego, M. The Cenozoic Lower Rhine Basin–rifting, sedimentation, and cyclic stratigraphy. *International Journal of Earth Sciences*, 94: 621–639, 2005. doi: 10.1007/s00531-005-0499-7.

Scherbaum, F., Hinzen, K.-G., and Ohrnberger, M. Determination of shallow shear wave velocity profiles in the Cologne, Germany area using ambient vibrations. *Geophysical Journal International*, 152(3):597–612, 2003. doi: 10.1046/j.1365-246X.2003.01856.x.

Schippkus, S., Garden, M., and Bokelmann, G. Characteristics of the ambient seismic field on a large-N seismic array in the Vienna basin. *Seismological Society of America*, 91(5):2803–2816, 2020. doi: 10.1785/0220200153.

Seppi, I., Tape, C., and Fee, D. Classification of Aircraft Types Using Seismic Data in Alaska. *The Seismic Record*, 5(4):330–340, 2025. doi: 10.1785/0320250035.

Sheng, Y. Seismic stereometry: an alternative two-station algorithm to seismic interferometry for analysing car-generated seismic signals. *Geophysical Journal International*, 235(1): 853–861, 2023. doi: 10.1093/gji/ggad287.

Stammler, K., Bischoff, M., Brüstle, A., Ceranna, L., Donner, S., Fischer, K., Gaebler, P., Friederich, W., Funke, S., Hartmann, G., Homuth, B., Knapmeyer-Endrun, B., Korn, M., Megies, T., Pilger, C., Plenefisch, T., Pustal, I., Rappsilber, I., Schmidt, B., Sonnabend, L., Stange, S., Wassermann, J., and Wegler, U. German seismic and infrasound networks contributing to the European integrated data archive (EIDA). *Seismological Research Letters*, 92 (3):1854–1875, 2021. doi: 10.1785/0220200401.

The ObsPy Development Team. ObsPy 1.4.0 (1.4.0) [Software], 2022. doi: 10.5281/zenodo.6645832.

Topsonic Systemhaus GmbH. TraVis Version 4.1.37, 2022. https://travis.koeln-bonn-airport.de. accessed 09/2023.

Tsuji, T., Kobayashi, T., Kinoshita, J., Ikeda, T., Uchigaki, T., Nagata, Y., Kawamura, T., Ogawa, K., Tanaka, S., and Araya, A. Lunar active seismic profiler for investigating shallow substrates of the Moon and other extraterrestrial environments. *Icarus*, 404: 115666, 2023. doi: 10.1016/j.icarus.2023.115666.

Turner, A. R., Hawthorne, J. C., and Gaddes, M. Stresses in the lunar interior: insights from slip directions in the A01 deep moonquake nest. *Journal of Geophysical Research: Planets*, 127(12): e2022JE007364, 2022. doi: 10.1029/2022JE007364.

Tyagunov, S., Hollnack, D., and Wenzel, F. Engineering-seismological analysis of site effects in the area of Cologne. *Natural Hazards*, 38:199–214, 2006. doi: 10.1007/s11069-005-8613-5.

Vrettos, C., Hardenberg, M., Becker, A., Knapmeyer-Endrun, B., Schlutz, J., and Uhlig, T. Dynamic properties of the EAC-1A lunar regolith simulant from resonant column tests. *Manuscript submitted to Planetary and Space Science*, 2026.

Wang, C., Jia, Y., Xue, C., Lin, Y., Liu, J., Fu, X., Xu, L., Huang, Y., Zhao, Y., Xu, Y., Gao, R., Wei, Y., Tang, Y., Yu, D., and Zou, Y. Scientific objectives and payload configuration of the Chang'E-7 mission. *National Science Review*, 11(2):nwad329, 12 2023. doi: 10.1093/nsr/nwad329.

Wang, H., Chen, Y., Min, R., and Chen, Y. Urban DAS data processing and its preliminary application to city traffic monitoring. *Sensors*, 22(24):9976, 2022. doi: 10.3390/s22249976.

Wang, X., Williams, E. F., Karrenbach, M., Herráez, M. G., Martins, H. F., and Zhan, Z. Rose Parade seismology: Signatures of floats and bands on optical fiber. *Seismological Research Letters*, 91 (4):2395–2398, 2020. doi: 10.1785/0220200091.

Wathelet, M. An improved neighborhood algorithm: Parameter conditions and dynamic scaling. *Geophysical Research Letters*, 35(9):L09301, 2008. doi: 10.1029/2008GL033256.

Wathelet, M., Guillier, B., Roux, P., Cornou, C., and Ohrnberger, M. Rayleigh wave three-component beamforming: signed ellipticity assessment from high-resolution frequency-wavenumber processing of ambient vibration arrays. *Geophysical Journal International*, 215(1):507–523, 2018. doi: 10.1093/gji/ggy286.

Wathelet, M., Chatelain, J.-L., Cornou, C., Giulio, G. D., Guillier, B., Ohrnberger, M., and Savvaidis, A. Geopsy: A user-friendly open-source tool set for ambient vibration processing. *Seismological Research Letters*, 91(3):1878–1889, 2020. doi: 10.1785/0220190360.

Wu, W., Zhan, Z., Panning, M., and Klesh, A. Fiber seismic network on the Moon. *Seismological Research Letters*, 95(4):2153–2163, 2024. doi: 10.1785/0220230067.

Yuan, S., Lellouch, A., Clapp, R. G., and Biondi, B. Near-surface characterization using a roadside distributed acoustic sensing array. *The Leading Edge*, 39(9):646–653, 2020. doi: 10.1190/tle39090646.1.

Zemeny, A., Sardisco, L., Quinteros, S., Mikesell, T. D., Pirrie, D., Rose, L., Cowley, A., and Manick, K. The Luna Analog Facility testbeds (ESA, EAC): contemporary characterization work of highland (lunar) and mare (EAC-1) lunar regolith simulants. *Frontiers in Space Technologies*, 5:1510635, 2024. doi: 10.3389/frspt.2024.1510635.

Zhai, Q., Husker, A., Zhan, Z., Biondi, E., Yin, J., Civilini, F., and Costa, L. Assessing the feasibility of Distributed Acoustic Sensing (DAS) for moonquake detection. *Earth and Planetary Science Letters*, 635:118695, 2024. doi: 10.1016/j.epsl.2024.118695.